Original Article

MOLECULAR METABOLISM

Differential cell type-specific function of the aryl hydrocarbon receptor and its repressor in diet-induced obesity and fibrosis

Frederike J. Graelmann[1,11], Fabian Gondorf[1,11], Yasmin Majlesain[1], Birte Niemann[2], Katarina Klepac[2], Dominic Gosejacob[2], Marlene Gottschalk[1], Michelle Mayer[1], Irina Iriady[1], Philip Hatzfeld[1], Sophie K. Lindenberg[1], Klaus Wunderling[3], Christoph Thiele[3], Zeinab Abdullah[4], Wei He[5], Karsten Hiller[5], Kristian Händler[6,7,8], Marc D. Beyer[6,9], Thomas Ulas[6,7], Alexander Pfeifer[2], Charlotte Esser[10], Heike Weighardt[1,10], Irmgard Förster[1,11,*], Laia Reverte-Salisa[1,11,]**

ABSTRACT

Objective: The aryl hydrocarbon receptor (AhR) is a ligand-activated transcription factor regulating xenobiotic responses as well as physiological metabolism. Dietary AhR ligands activate the AhR signaling axis, whereas AhR activation is negatively regulated by the AhR repressor (AhRR). While AhR-deficient mice are known to be resistant to diet-induced obesity (DIO), the influence of the AhRR on DIO has not been assessed so far.
Methods: In this study, we analyzed AhRR$^{-/-}$ mice and mice with a conditional deletion of either AhRR or AhR in myeloid cells under conditions of DIO and after supplementation of dietary AhR ligands. Moreover, macrophage metabolism was assessed using Seahorse Mito Stress Test and ROS assays as well as transcriptomic analysis.
Results: We demonstrate that global AhRR deficiency leads to a robust, but not as profound protection from DIO and hepatosteatosis as AhR deficiency. Under conditions of DIO, AhRR$^{-/-}$ mice did not accumulate TCA cycle intermediates in the circulation in contrast to wild-type (WT) mice, indicating protection from metabolic dysfunction. This effect could be mimicked by dietary supplementation of AhR ligands in WT mice. Because of the predominant expression of the AhRR in myeloid cells, AhRR-deficient macrophages were analyzed for changes in metabolism and showed major metabolic alterations regarding oxidative phosphorylation and mitochondrial activity. Unbiased transcriptomic analysis revealed increased expression of genes involved in *de novo* lipogenesis and mitochondrial biogenesis. Mice with a genetic deficiency of the AhRR in myeloid cells did not show alterations in weight gain after high fat diet (HFD) but demonstrated ameliorated liver damage compared to control mice. Further, deficiency of the AhR in myeloid cells also did not affect weight gain but led to enhanced liver damage and adipose tissue fibrosis compared to controls.
Conclusions: AhRR-deficient mice are resistant to diet-induced metabolic syndrome. Although conditional ablation of either the AhR or AhRR in myeloid cells did not recapitulate the phenotype of the global knockout, our findings suggest that enhanced AhR signaling in myeloid cells deficient for AhRR protects from diet-induced liver damage and fibrosis, whereas myeloid cell-specific AhR deficiency is detrimental.

Keywords Metabolic dysfunction; Indole-3-carbinol; Collagen deposition; Energy expenditure; Macrophage metabolism; Hepatic steatosis

[1]Immunology and Environment, Life and Medical Sciences (LIMES) Institute, University of Bonn, Germany [2]Institute of Pharmacology and Toxicology, University Hospital Bonn, University of Bonn, Germany [3]Biochemistry & Cell Biology of Lipids, Life and Medical Sciences (LIMES) Institute, University of Bonn, Germany [4]Institute of Molecular Medicine and Experimental Immunology, University Hospital Bonn, University of Bonn, Germany [5]Braunschweig Integrated Centre of Systems Biology (BRICS), Technische Universität Braunschweig, Braunschweig, Germany [6]PRECISE Platform for Single cell Genomics and Epigenomics at the German Center for Neurodegenerative Diseases and the University of Bonn and West German Genome Center, Bonn, Germany [7]Genomics and Immunoregulation, Life and Medical Sciences (LIMES) Institute, University of Bonn, Germany [8]Institute of Human Genetics, Universitätsklinikum Schleswig-Holstein, University of Lübeck and University of Kiel, 23562 Lübeck, Germany [9]Immunogenomics & Neurodegeneration, German Center for Neurodegenerative Diseases, Bonn, Germany [10]IUF-Leibniz Research Institute for Environmental Medicine gGmbH, Düsseldorf, Germany

[11] Equal contribution.

*Corresponding author. Immunology and Environment, LIMES Institute, Carl-Troll-Straße 31, 53115 Bonn, Germany. E-mail: irmgard.foerster@uni-bonn.de (I. Förster).

**Corresponding author. Immunology and Environment, LIMES Institute, Carl-Troll-Straße 31, 53115 Bonn, Germany. E-mail: laia@uni-bonn.de (L. Reverte-Salisa).

Received March 6, 2024 • Revision received May 2, 2024 • Accepted May 25, 2024 • Available online 29 May 2024

https://doi.org/10.1016/j.molmet.2024.101963

1. INTRODUCTION

The aryl hydrocarbon receptor (AhR) is a sensor of polyaromatic chemicals, including environmental toxins (xenobiotic ligands), phytochemicals, and microbial or endogenous metabolites (natural ligands) [1–3]. Upon ligand binding and activation, AhR translocates from the cytoplasm into the nucleus for regulation of target gene expression. Transcriptional regulation of gene expression through the AhR has a major impact on immunity [4–6] as well as cellular and systemic metabolism [7–9]. While high-dose exposure with 2,3,7,8-tetrachlorodibenzo-p-dioxin (TCDD) causes hepatic steatosis [10–12] and wasting syndrome [13,14] in rodents, chronic low-dose exposure to industrial pollutants has been implicated in the development of obesity and insulin resistance [15–18]. Mice with a complete deficiency of the AhR [19] or those bearing a low-affinity AhR mutant [8] have been shown to be protected from hepatic steatosis and diet-induced obesity (DIO). Such resistance was not or only partially seen in animals with a hepatocyte-specific AhR deficiency [20], while mice with an adipocyte-specific knockout of the AhR show a sexually dimorphic effect on weight gain when fed a HFD [15,21]. These findings indicate an important yet cell type-specific function of the AhR that may either enhance or protect from DIO and metabolic dysregulation. Expression of a constitutively active mutant of the AhR under control of the fatty acid binding protein (FABP) promoter in the liver caused hepatic steatosis but protected the animals from DIO due to enhanced expression of CD36 and production of the hepatokine fibroblast growth factor 21 (FGF21) as a direct transcriptional target of AhR [12,22]. Furthermore, several key metabolic enzymes involved in lipid metabolism were found to be transcriptionally regulated through the AhR [23,24].

Considering the major impact of AhR activation on cellular metabolism as well as immune regulation by xenobiotic and endobiotic ligands [1,3,25,26], the AhR signaling pathway is tightly regulated through feedback inhibition. Enzymes of the Cytochrome p450 monooxygenase (CYP) family, such as CYP1A1, CYP1A2, and CYP1B1, are strongly induced by AhR activation and rapidly metabolize AhR ligands leading to a shut-down of this signaling pathway [4,27,28]. Two other target genes of the AhR encode the TCDD-inducible poly (ADP-ribose) polymerase (TiPARP) and the AhRR, which turn down AhR signaling by different means, either through enhanced ribosylation-mediated protein degradation of the AhR or by competition for binding to AhR nuclear translocator (ARNT), respectively [1,29–31].

We previously generated an *Ahrr* reporter allele in mice, in which the enhanced green fluorescent protein (EGFP) is expressed under the control of the endogenous *Ahrr* promoter. Using these AhRR/EGFP reporter mice, we demonstrated that the AhRR is mainly expressed in immune cells of the skin and intestinal mucosa, including myeloid cells, innate lymphoid cells, and several T cell subsets [32]. No notable expression of the AhRR could be detected in intestinal epithelial cells at steady state or following systemic AhR stimulation, whereas other AhR target genes are known to be expressed at this site [4,33]. Thus, the AhRR appears to play a predominant role in regulating AhR activation in a cell type- or organ-specific manner, in particular in hematopoietic cells [32,34,35]. Functionally, AhRR-dependent regulation of AhR activity was shown to be important for the balancing of cytokine production by myeloid cells and T cells in the context of inflammation [32]. Recently, it was shown that AhRR deficiency decreases intestinal intraepithelial lymphocyte (IEL) numbers in an oxidative stress-dependent manner, facilitating intestinal infection and inflammation [36].

Tissue-resident immune cells have been demonstrated to be essential regulators of lipid metabolism, energy consumption, and thermogenesis in adipose tissues [37–42]. Therefore, the regulation of AhR function through the AhRR, which is predominantly expressed in immune cells, may represent an important rheostat of lipid metabolism. Macrophages, in particular, are known to control homeostasis in metabolic organs such as the liver [43–45] and adipose tissue [46–48], depending on their activation status [41,42,49].

In the present study, we evaluated the relevance of the AhRR as well as the dietary induction of AhR signaling for systemic and cellular metabolism. We also determined the sensitivity of complete and myeloid cell-specific AhRR-deficient mice to DIO in direct comparison to AhR deficiency.

2. MATERIALS AND METHODS

2.1. Animals and experimental animal procedures

All mice were bred and maintained in individually ventilated cages under specific pathogen–free conditions. $AhRR^{-/-}$, $AhRR^{fl/fl}$, $AhRR^{fl/fl}LysM^{Cre}$, and $AhR^{-/-}$ mice [50] were bred at the animal facility of the LIMES Institute, Bonn, Germany. $AhR^{fl/fl}LysM^{Cre}$ mice were bred at the animal facility of the IUF, Düsseldorf, Germany. In all experiments with myeloid cell-specific conditional knockout mice, the $LysM^{Cre}$-knockin allele was heterozygous (Cre/+). WT and littermate mice served as controls. All mice were on a C57BL/6JRcc background.

Seven to thirteen-week-old male mice were used for the experiments and were bred according to German guidelines for animal care. For individual *in vivo* experiments, mice were no more than 3 weeks different in age and randomly assigned to treatment groups. All experiments were performed according to German and Institutional guidelines for animal experimentation (permits: AZ 84–02.04.2015.A043, 81–02.04.2019.A262 and 81–02.04.2017.A435) and were approved by the government of North Rhine-Westphalia (Germany).

For dietary intervention studies, mice were exposed to a purified diet or with 2 g/kg indole-3-carbinole (I3C)-supplemented control diet (CD/CD+I3C, 13 kJ% Fat, Cat No.: D12450 LS ssniff EF) or a purified or with 2 g/kg I3C-supplemented high fat diet (HFD/HFD+I3C, 60 kJ% fat, Cat. No.: D12492 ssniff EF) *ad libitum*. The body weight was assessed weekly. After 14 weeks of feeding, the mice were analyzed.

2.2. Generation of $AhRR^{fl/fl}$ mice

To generate AhRR-floxed mice, loxP recognition sequences were introduced in the second and third intron of the *Ahrr* gene, flanking the third exon, which contains the bHLH domain of the AhRR essential for DNA binding [51,52]. An frt-flanked neomycin resistance gene was inserted behind the 5′ loxP site to allow for positive selection of the targeted ES cells. After electroporation of the targeting vector into HM-1 ES-cells (Sv129/OlaHsd), selected clones were screened by PCR and Southern blot using a 3′ flanking probe. Successfully recombinant clones were injected into C57BL/6JRcc blastocysts. Germline transmission was proven by PCR analysis. Mice were backcrossed to C57BL/6JRcc for 8 generations.

The frt-flanked neomycin resistance cassette was deleted by directly introducing flippase (flp) mRNA into fertilized oocytes of homozygous AhRR-floxed ($AhRR^{fl/fl}$) mice. StemMACS Flp Recombinase mRNA (130-106-769, Miltenyi Biotec GmbH) was introduced by electroporation (7 square wave pulses of 30 V, 3 ms, 0.1s pause) using a GenePulser Xcell electroporator (BioRad) and a 1 mm cuvette (BioRad). Differentiated 2-cell stage embryos were transferred into pseudopregnant females BALB/cAnNCrl (50%) C57BL/6NCrl (50%). Offspring was screened by PCR and sequencing of the locus for successful removal of the neomycin cassette. The targeting strategy is depicted in Fig. S3A.

To generate AhRR-deficient mice, $AhRR^{fl/fl}$ mice were bred to Cre-deleter mice. Deletion of the third exon of the *Ahrr* was demonstrated by PCR analysis and the Cre allele was removed by backcrossing the mice to C57BL/6JRcc mice.
To delete AhRR in myeloid cells, $AhRR^{fl/fl}$ mice were crossed to $LysM^{Cre}$ mice [53]. The deletion efficiency was evaluated by qPCR. A control fragment, giving rise to a signal in both $AhRR^{fl/fl}$ and $LysM^{Cre}$-deleted strains (primers House 350 BP) and a fragment spanning the deleted allele after Cre recombination (primers dCRE) was amplified from genomic DNA of BMMΦ of $AhRR^{fl/fl}$ and $AhRR^{fl/fl}LysM^{Cre}$ mice. A standard reaction using WT and AhRR-deficient genomic DNA was included.
Primers:
House350BP For AATGGCCTGACACCCCACTC
House350BP Rev TCCAACGTGACCCTTCCACC
dCRE For GAGGCCAGATGGAACTGTCT
dCRE Rev GGTCAGCCAACAGCCATCTA

2.3. Glucose and insulin tolerance test

Glucose tolerance tests (GTT) or insulin tolerance tests (ITT) were performed at week 12 of feeding. A drop of blood from the nicked tail vein was used to determine the basal glucose concentration using AccuChec Instant test strips (C216796165-IMP, Roche) after 6 h of fasting for GTT and without fasting for ITT. Then, mice were injected intraperitoneally with 0.25 mg/L glucose at a dose of 2 g/kg of body weight or 0.09375 U/mL insulin at a dose of 0.75 U/kg of body weight, respectively. Blood glucose levels were subsequently measured at 15, 30, 60, 90, 120, and 150 min post-injection.

2.4. Measurement of serum and plasma parameters

Piccolo Express Chemistry Analyzer (Abaxis Inc.) and Reflotron Plus Analyzer (Roche Diagnostics) were used to measure the concentration of blood serum and plasma parameters. Blood samples were collected into EDTA tubes from the *vena facialis* of experimental animals. Serum was tested for Alanine Aminotransferase (ALT/GPT, Ref 10745138), and Cholesterol (Ref 10745065) levels using respective test strips (Roche Diagnostics) following manufacturer's instructions. Using the Piccolo analyzer, the Lipid Panel Plus (Ref 400—1030) was obtained.

2.5. Macrophage staining

Paraffin-embedded samples from gonadal white adipose tissue (WATg) were sectioned and deparaffinized. Antigen retrieval was performed with 10 mM Sodium Citrate Buffer (pH 6) at 85 °C for 50 min. After treatment with BloxAll Blocking Solution (VectorLabs, Cat.-No. SP-6000), samples were blocked with 2.5% goat serum and stained with rat anti-F4/80 (clone A3-1, Santa Cruz, Cat.-No. sc-59171) and subsequently HRP-coupled goat anti rat IgG secondary antibody (ImmPRESS Goat Anti-Rat IgG Polymer Kit Peroxidase, VectorLabs, Cat.-No. MP7404). The HRP substrate reaction was performed with DAB (ImmPACT DAB Substrate Kit, Peroxidase, Cat.-No. SK-4105), samples were counterstained with Hemalaun, and mounted with VectaMount Permanent Mounting Medium. Images were acquired with a Keyence BZ-9000 Microscope (Keyence Corporation).

2.6. Oil Red O staining

Livers were fixed in 4% paraformaldehyde (PFA) for at least 4 h, dehydrated by treatment with ascending concentrations of D-Sucrose for at least 2 h per solution, and embedded in Tissue Tek. 10 μm sections were washed in Formalin, rinsed in 60% Isopropanol, and stained in freshly prepared Oil Red O staining solution (5 g/L in Isopropanol). The samples were counterstained with Hemalaun and mounted with Kaiser's glycerol gelatin with Phenol. Randomized images were obtained using a Keyence BZ-9000 microscope.
Quantitative analysis was performed using Fiji (Rasband, W.S., ImageJ, U. S. National Institutes of Health, https://imagej.nih.gov/ij/, 1997—2018). Thereby, the tissue was distinguished from background signal in the pictures and the mean intensity of red signal in the tissue was calculated. Subsequently, the Optical Density (OD) was calculated from the values of mean intensity, normalizing the mean intensity on the maximal intensity (value of maximal intensity = 255) with the following formula: OD = log(Maximal Intensity/Mean Intensity). The script for quantification is provided upon request.

2.7. Culture of bone marrow-derived macrophages (BMMΦ)

For isolation of BMMΦ, the femur and tibiae of mice were flushed with sterile PBS. The bone marrow cells were cultured and differentiated at 37 °C and 5% CO_2 in RPMI medium supplemented with 10—15% supernatant of L929 cells, 10% FCS, penicillin/streptomycin, 50 μM β-mercaptoethanol and 2 mM L-Glutamine. Fresh medium was added on day 4 of the culture. After seven days, the cells were harvested and used for downstream readouts.

2.8. Isolation of liver macrophages

Liver macrophage isolation was performed as previously described [54]. In brief, livers were perfused with EDTA and Heparin in HBSS and subsequently with 50 mg/mL collagenase and 0.125 mM $CaCl_2$ in Williams E medium via the portal vein. After perfusion, the liver was removed from the diaphragm and put into a beaker glass to shake the organ. The resulting cell suspension was transferred into a 50 mL reaction tube and centrifuged for 2 min at 20 g. The supernatant of the first centrifugation, containing the Kupffer cells, was re-centrifuged at 500 g for 10 min. The supernatant was subjected to Magnetic Activated Cell Sorting (MACS) using CD11b magnetic microbeads (Order No. 130-093-634, Miltenyi Biotec) according to the manufacturer's instructions and over LS columns after red blood cell lysis. After washing, the eluted cells were plated to a Seahorse 96 well cell plate in a range from 100,000 to 200,000 cells/well.

2.9. Generation of Fetal Liver Macrophage (FLiM) cell lines

FLiM cells were generated as described in Fejer et al., 2013 [55]. Briefly, single cell suspensions of fetal livers of E13.5 mouse embryos were prepared and cultured in T75 flasks in FLiM medium (RPMI 1640, 10% FCS, 2 mM L-Glutamine, 100 U/mL Penicillin/Streptomycin, 50 μM β-mercaptoethanol with 2% supernatant of granulocyte-macrophage colony-stimulating factor (GM-CSF) transfected X63Ag8—653-cells). When a stable proliferation rate was reached, cells were split 1:20 based on confluence every 6—7 days, while fresh medium was added 2—3 days after splitting.

2.10. Seahorse Assay (Mito Stress Test)

One day before the assay (BMMΦ) or on the day of the assay (liver macrophages), 1—2 x 10^5 cells were seeded in XF96 cell culture microplates (Seahorse Bioscience). The Sensor Cartridge was prepared according to the manufacturer's instructions. One hour prior to the assay, growth medium was discarded and replaced by Seahorse Assay XF RPMI assay medium (pH 7.4), and the plate was incubated for 60 min at 37 °C. Mito Stress Test inhibitor stock solutions were adjusted to appropriate concentrations and pipetted into the ports of the Sensor Cartridge (Port A: 20 μL of 10 μM Oligomycin; Port B: 22 μL of 40 μM FCCP; Port C: 25 μL of 5 μM Rotenone/Antimycin A). A Seahorse Bioscience XFe96 Analyzer was used to measure extracellular acidification rates (ECAR) and oxygen consumption rates (OCR)

every 3 min. After Seahorse measurement, cell numbers were normalized using the CyQuant NF Cell Quantification kit (Thermo Fisher Scientific).

2.11. ROS assay

FLiM cells were seeded in FLiM medium at a concentration of 1–3 x 10^5 cells/mL in a white 96 well plate at 37 °C 5% CO_2. After 24 h the plate was centrifuged at 400 g for 5 min, the medium was discarded and 170 μL/well fresh FLiM medium was added. Directly before measuring, 30 μL/well of the Luminol mix containing 80 U/mL Horseradish peroxidase (Merck) and 8 mM Luminol (AppliChem Life Science) in Borate buffer (0.2 M H_3BO_3 0.02 M $Na_2B_4O_7x10H_2O$) was added including either 0.4 mg/mL Zymosan (Sigma Aldrich) or PBS for control samples. ROS production was measured in relative luminescence units (RLU) via a luminometer (Berthold Technologies) for a period of 30–60 min. Area under the curve was calculated.

2.12. Flow cytometric analysis of mitochondrial membrane potential using Tetramethylrhodamine Methyl Ester (TMRM)

0.75 x 10^6 FLiM cells were seeded in FLiM medium in a six well plate and incubated overnight at 37 °C 5% CO_2. The Mitoprobe TMRM kit (Thermo Fisher Scientific) was used according to manufacturer's instructions. Prior to flow cytometric analysis, cells were harvested, washed with PBS, and then resuspended in 500 μL PBS before measuring TMRM intensity using the PE bandpass filter of a FACSCanto (BD Biosciences).

2.13. Metabolic cages and determination of body composition

2.13.1. Energy expenditure

Oxygen consumption was measured for 120 s per cage during 24 h using Phenomaster (TSE Systems). All mice were maintained on a daily cycle of 12-hours light (06:00–18:00 h) and 12-hours darkness (18:00–06:00 h), at 23 ± 1 °C and were allowed free access to chow and water.

2.13.2. Body composition analysis

Body composition was analyzed using a table Bruker Minispec.

2.14. H&E and Sirius Red staining

WATg and liver were fixed in PBS containing 4% PFA overnight and dehydrated using ethanol. Dehydrated tissues were embedded in paraffin. Paraffin-embedded samples from WATg and liver were cut in 5 μm sections. Sections were deparaffinized and hydrated to distilled water.

Haematoxylin and eosin (H&E): Sections were stained with Hemalaun for 3 min and rapidly washed with distilled water. Staining with eosin was performed right after by incubating the tissue sections in eosin for 3 min and washing with distilled water. Following dehydration, samples were mounted in Entellan (107960, Sigma-Aldrich) and dried overnight. Images were acquired with a Keyence BZ-9000 Microscope (Keyence Corporation). Blinded manual scoring of liver steatosis was performed using the grading from Sethunath et al. [56].

Sirius Red: Sections were covered and incubated for 60 min with Picrosirius Red solution (SRS500, ScyTek Laboratories). Slices were quickly rinsed in a 0.5% acetic acid solution (Cat #AAD, ScyTek), followed by a quick rinse in 100% ethanol. Samples were embedded in Euparal (Art. No. 7356.1, Roth) and dried overnight. Images were acquired with a Keyence BZ-9000 Microscope (Keyence Corporation). The Fibrosis Score of stained WATg samples was assessed according to Lassen et al. [57].

2.15. RNA isolation and qRT-PCR

RNA from WATg and liver was isolated as described [58]. Final concentration of RNA was quantified using a Nanodrop Spectrophotometer. First-strand cDNA was synthesized from 1000 ng of total RNA using mixture of oligo(dT)12–18 primers and Superscript reverse transcriptase (Thermo Fisher Scientific).

mRNA expression was assessed by qRT-PCR using a Real-Time system CFX96 (BioRad) and Absolute qPCR SYBR Green ROX mix (Thermo Fisher Scientific). Quantification of mRNA levels was performed based on the crossing point values of the amplification curves using the second derivative maximum method. mRNA expression levels were normalized to *Hprt* and were displayed as fold change relative to samples of control mice used as calibrator.

The primer sequences are shown in the following table:

Sequences of primers used for RT-PCR analysis.

Gene name	Species		Primer sequence (5' – 3')
Hprt	Mouse	*Forward*	GTCCCAGCGTCGTGATTAGC
		Reverse	TCATGACATCTCGAGCAAGTCTTT
Pparγ	Mouse	*Forward*	ACAAGACTACCCTTTACTGAAATTACCAT
		Reverse	TGCGAGTGGTCTTCCATCAC
Fabp4	Mouse	*Forward*	GCGTGGAATTCGATGAAATCA
		Reverse	CCCGCCATCTAGGGTTATGA
Adipoq	Mouse	*Forward*	GCCGTTCTCTTCACCTACGA
		Reverse	CATACACCTGGAGCCAGACTT
Cd36	Mouse	*Forward*	TGAGACTGGGACCATTGGTGAT
		Reverse	CCCAAGTAAGGCCATCTCTACCAT
Fasn	Mouse	*Forward*	GCTGCTGTTGGAAGTCAGC
		Reverse	AGTGTTCGTTCCTCGGAGTG
Fsp27	Mouse	*Forward*	CAAGGCCAAGCGCATCGT
		Reverse	TGCCAAGCAGCATGTGACCG
Col1a1	Mouse	*Forward*	GAGATGATGGGGAAGCTGGC
		Reverse	CTCGGTGTCCCTTCATTCCG
Col6a1	Mouse	*Forward*	CAGGTACTACCGGTGTGACC
		Reverse	GAAGTACTTGACCGCATCCAC
Fn1	Mouse	*Forward*	CTCCGAGACCAGTGCATCG
		Reverse	GAATCTTGGCACTGGTCAATGG
Loxl2	Mouse	*Forward*	CTGCCTGGAGGACACTGAGT
		Reverse	CGGTGATGTCTATCCACTGGC
Mcp1	Mouse	*Forward*	AGGTCCCTGTCATGCTTCT
		Reverse	GGATCATCTTGCTGGTGAAT
Tnfa	Mouse	*Forward*	TCTTCTCATTCCTGCTTGTGG
		Reverse	GGTCTGGGCCATAGAACTGA

2.16. Metabolite extraction from plasma samples

Extraction was performed as previously described [59,60]. Briefly, 20 μL plasma sample was added to 180 μL ice-cold methanol:H_2O (8:1) containing 2 μg/mL D6-pentanedioic acid (C/D/N Isotopes, Quebec, Canada) as internal standard. The mixture was vortexed at 1400 rpm for 10 min at 4 °C and centrifuged at 17,000 g for 10 min at 4 °C. 80 μL supernatant was transferred into glass vials compatible with gas chromatography and then dried under vacuum at 4 °C in a CentriVap Concentration System (Labconco, Kansas City, Missouri).

2.17. GC-MS measurement and data analysis

GC-MS measurement of relative metabolite levels was performed as described [61], using an Agilent 7890B gas chromatograph equipped with a 30 m DB-35 ms and 5 m Duraguard capillary column (Agilent, Santa Clara, California) for separation of derivatized metabolites, and an Agilent 5977B MSD system (Agilent) for measurement of metabolites. Briefly, dried metabolite extracts were derivatized with equal amounts of

methoxylamine (20 mg/mL in pyridine, both Sigma-Aldrich, Steinheim, Germany) and MSTFA or MTBSTFA (Restek Corporation, Bellefonte, Pennsylvania) before injection into the GC-MS system. Measurements were carried out in either full scan or selected ion mode. Processing of chromatograms and relative quantification of metabolites were performed using the Metabolite Detector software [62].

2.18. Transcriptome analysis

Cells were lysed using Qiazol (Qiagen) for RNA isolation, and RNA was extracted using the miRNeasy kit (Qiagen), following the manufacturer's instructions. Polyadenylated RNA was then enriched from total RNA using Oligo-dT-coupled magnetic beads. The RNA was fragmented and transformed into double-stranded cDNA libraries using the TruSeq RNA Sample Preparation Kit v2 (Illumina), following manufacturer's protocol. cDNA fragments, favoring 200 bp, were selected and purified. Sequencing was done on a HiSeq1500 device in a 75bp single-end run, after cluster generation on a cBot station (Illumina). Raw sequencing reads underwent quality control with fastQC 0.11.9 (https://www.bioinformatics.babraham.ac.uk/projects/fastqc/) and were summarized using MultiQC v1.14 (https://multiqc.info/). The 75 bp single-end reads were trimmed using fastp v0.20.0 and aligned to the murine mm10 vM32 reference genome from GENCODE using STAR v2.7.10b (https://github.com/alexdobin/STAR, [63]) with –quantMode GeneCounts. Aligned reads sorted by coordinates were indexed using samtools v1.16.1. The alignment process was managed using SnakeMake 7.20.0 (https://snakemake.github.io/, [64]). Subsequent data analysis was conducted in R version 4.2.2 RStudio 2023.09.0 Build 303, mainly utilizing the DESeq2 version 138.3 R package [65]. Raw counts were imported into R, and a DESeq object was created using the DESeqDataSetFromMatrix function. Genes with fewer than 10 total counts were omitted, leaving 16,111 genes for analysis. Size factors and dispersions were estimated per gene using the default settings for DESeq2. Unwanted variations, like technical variance from donors, were addressed in the normalization process or removed using surrogate variable analysis (sva) [66]. The rlog-transformed expression values, adjusted for surrogate variables identified by sva, were processed with the "removeBatchEffect" function from the limma package [67]. Differential expression analysis was conducted using DESeq2, incorporating SV1 and SV2 into the design model for comparing $AhRR^{-/-}$ samples to WT controls. This analysis, which applied a fold change (FC) threshold of 1.5, utilized the 'apeglm' method for shrinkage of estimates and the Independent Hypothesis Weighting (IHW) approach for multiple testing correction, identified 312 genes as upregulated and 360 genes as downregulated at an adjusted p-value cutoff of 0.05. Gene set enrichment analysis (GSEA) [68] was carried out on the transcriptome data for all Hallmark gene sets [69], comparing $AhRR^{-/-}$ versus WT controls. Only gene sets with an adjusted p-value under 0.05 (Benjamini-Hochberg correction) were considered and visualized. Differentially expressed genes were filtered for transcription factors [70], surface and secretome markers from the Human Protein Atlas [71], and metabolism genes based on literature. The top 20 genes from each category were visualized in a heat map. Sequencing data associated with this paper has been submitted to NCBI's GEO repository under the accession number GSE254369.

3. RESULTS

3.1. AhRR-deficient mice are partially resistant to diet-induced obesity

Here we asked whether enhanced AhR activation by deletion of the AhRR, a negative regulator of AhR signaling, might impact the induction of DIO and the resulting disturbances in metabolism. Activation of the AhR by xenobiotic or endogenous ligands is likely to contribute to DIO, as AhR-deficient mice or mice expressing the low-affinity AhR are protected from diet-induced weight gain and liver steatosis [8,19]. In line, the inhibition of AhR activation by CH-223191 led to the same effect [72]. When global AhRR-deficient mice were fed with HFD for 14 weeks, their weight gain was significantly lower than that of WT control mice (Figure 1A). Blood glucose levels were significantly lower in AhRR-deficient mice compared to WT mice after glucose and insulin stimulation (Figure 1B). In addition, total serum cholesterol levels were significantly reduced in mice lacking the AhRR (Figure 1C). In line with these results, $AhRR^{-/-}$ HFD-fed mice had higher O_2 consumption at room temperature (Figure 1D). As expected, the total fat mass was increased in HFD WT compared to CD mice, but this weight gain was strongly decreased in HFD $AhRR^{-/-}$ compared to WT HFD mice (Figure 1E). In alignment with the total fat mass, the weight of WATg was increased by 198% after HFD feeding, while AhRR-deficient mice had 53.4% less WATg compared to WT HFD mice (Figure 1F). Moreover, this reduction in WATg weight was accompanied by a reduced adipocyte size in mice lacking AhRR (Figure 1G). This indicates that deficiency of the AhRR protects from weight gain and enlargement of adipose tissue after HFD feeding in mice. Another hallmark of DIO is liver steatosis. Here, liver weight was increased in WT mice after HFD feeding. In contrast, the liver weight was unaltered in HFD-fed AhRR-deficient mice compared to CD-fed mice (Figure 1H). Histological analysis revealed that lipid droplet accumulation in the liver was reduced in HFD-fed AhRR-deficient mice. Also, a reduced level of neutral lipids in the liver tissue was demonstrated by reduced staining intensity of Oil Red O (ORO) (Figure 1I—J). Accordingly, while serum levels of alanine aminotransferase (ALT) were enhanced in HFD-fed WT mice, indicating liver damage, this was not observed in HFD-fed AhRR-deficient mice (Figure 1K).

As activation of the AhR by feeding I3C protects mice from DIO affecting body weight gain and lipid accumulation [73], we wondered whether additional AhR activation with I3C affects DIO in AhRR-deficient mice. As expected, WT mice fed HFD supplemented with 2 g/kg I3C gained less weight compared to WT mice fed HFD only (Figure 1L). AhRR-deficient mice again had reduced weight gain, with no notable further reduction of weight gain after feeding the I3C-supplemented HFD (Figure 1L). The lower weight gain in WT mice fed I3C-supplemented HFD was only marginally reflected by a reduced accumulation of lipid droplets in the liver. AhRR-deficient mice, in contrast, already show reduced lipid buildup after feeding HFD without further reduction after I3C supplementation (Figure 1M). Similar to published data [74], metabolomic analysis of the plasma revealed an increase in TCA cycle intermediates in WT HFD mice hinting to metabolic dysfunction upon 14 weeks of HFD, which was absent in HFD AhRR-deficient mice and in both groups fed an I3C-supplemented HFD (Figure 1N). As expected, AhR-deficient mice only moderately gained weight after HFD feeding, while supplementation with I3C did not influence body- or liver weight gain in these mice, indicating that the observed effect of I3C supplementation is indeed AhR-dependent (Fig. S1A). In line, I3C supplementation did not elicit any changes in the plasma metabolome of $AhR^{-/-}$ mice (Fig. S1B). In conclusion, the above findings indicate that metabolic alterations induced by DIO can be reverted by specific activation of the AhR.

3.2. AhRR-deficient macrophages display an altered metabolic and gene expression profile

Since AhRR expression is most prominent in immune cells, such as myeloid cells [32,75], we assessed whether AhRR expression

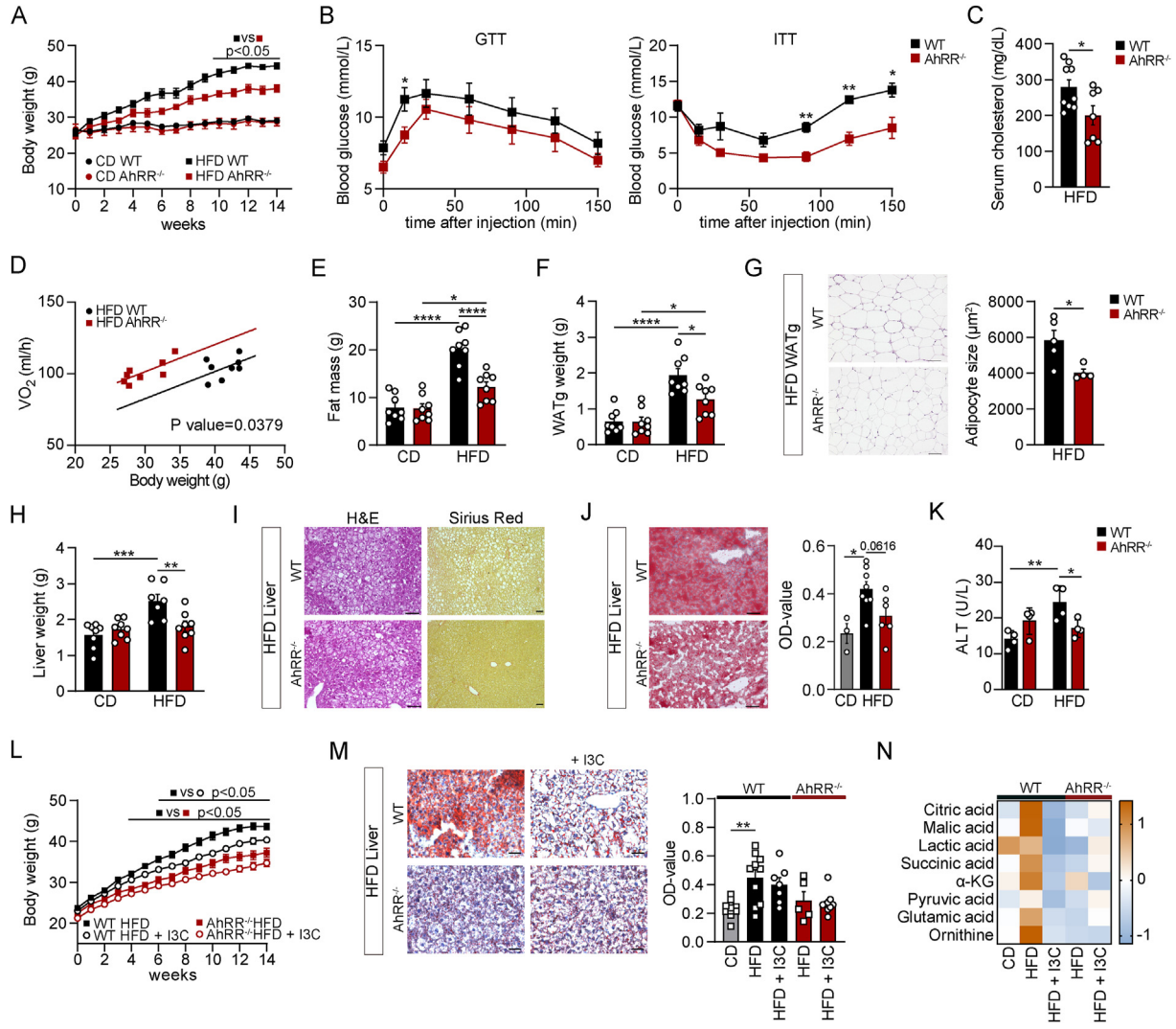

Figure 1: AhRR-deficient mice are partially resistant to diet-induced obesity. (**A**) Body weight of wild-type (WT) and AhRR-deficient mice fed CD or HFD for 14 weeks; n = 8 (CD WT), n = 6 (HFD WT), n = 5 (CD, HFD AhRR$^{-/-}$). (**B**) Blood glucose levels during a glucose tolerance test -GTT- (left panel) and insulin tolerance test -ITT- (right panel) after 12 weeks on HFD; n = 11 (GTT WT), n = 10 (GTT AhRR$^{-/-}$), n = 5 (ITT WT, ITT AhRR$^{-/-}$). (**C**) Total serum cholesterol levels after 14 weeks on HFD; n = 9 (WT), n = 7 (AhRR$^{-/-}$). (**D**) Analysis of covariance (ANCOVA) (non-linear fit) of oxygen consumption/body weight (BW); n = 8 for both groups. (**E**) Total body fat mass assessed by NMR; n = 8 for both groups. (**F**) WATg weight; n = 8 for both groups. (**G**) Representative H&E staining. Scale bars, 80 µm (left panel). Right, quantification of adipocyte size of the WATg of HFD mice; n = 5 (WT), n = 4 (AhRR$^{-/-}$). (**H**) Liver weight; n = 8 (CD WT, CD AhRR$^{-/-}$, HFD AhRR$^{-/-}$), n = 7 (HFD WT). (**I**) Representative H&E (left panel) and Sirius Red (right panel) staining of liver sections. Scale bars, 100 µm. (**J**) Representative Oil Red O (ORO) and Hemalaun staining of liver sections of WT and AhRR-deficient mice after HFD. Scale bars, 80 µm (left panel). Right, quantification of ORO stain, n = 3 (CD WT), n = 8 (HFD WT), n = 6 (HFD AhRR$^{-/-}$). (**K**) Serum Alanine transaminase (ALT) concentration of WT and AhRR-deficient mice fed either CD or HFD for 14 weeks; n = 4 for all groups. (**L**) Body weight of WT and AhRR-deficient mice fed a HFD supplemented with or without indole-3 carbinole (I3C) for 14 weeks; n = 20 (WT HFD), n = 15 (WT HFD + I3C), n = 15 (AhRR$^{-/-}$ HFD), and n = 14 (AhRR$^{-/-}$ HFD + I3C). (**M**) Representative ORO and Hemalaun staining of liver sections of WT and AhRR$^{-/-}$ mice after HFD ± I3C. Scale bars, 100 µm (left panel). Right, ORO staining quantification of liver sections; n = 10 (WT CD, HFD), n = 7 (WT HFD + I3C), n = 5 (AhRR$^{-/-}$ HFD), n = 9 (AhRR$^{-/-}$ HFD + I3C). (**N**) z-scored intensity values of representative TCA-metabolites found in plasma of mice after 14 weeks of CD or HFD ± I3C; n = 3–5. *p < 0.05, **p ≤ 0.01, ***p ≤ 0.001. Significance was determined using unpaired two-tailed t-tests (A, B, C, G) and one-way analysis of variance (ANOVA) with Tukey's multiple-comparison test (E, F, H, K and M) or with Dunnett's multiple comparisons test (J). Two-way analysis of variance (ANOVA) with Tukey's multiple-comparison test (L). Data are mean ± s.e.m.

modulates the metabolism and gene expression profiles in macrophages. For this purpose, we compared the transcriptome profiles using WT and AhRR-deficient long-term Fetal Liver Macrophage (FLiM) cell lines [55]. AhRR$^{-/-}$ FLiM cells showed a profound alteration in their transcriptional profile in comparison to WT FLiM cells (Figure 2A–B, S2A) with a total of 672 differentially expressed genes (DEGs) (312 up, 360 down). Hallmark Gene Set enrichment analysis (GSEA) was performed on result of the DEG analysis comparing AhRR$^{-/-}$ vs WT FLiM cells. This analysis revealed an enrichment for Myc- and mTORC1 pathways known to control protein synthesis, metabolism, and mitochondrial biogenesis [76,77] in AhRR$^{-/-}$ compared to WT FLiM cells (Figure 2C). Markedly, genes involved in fatty acid and lipid mediator synthesis (*Acaca, Elovl6, Acly, Ch25h*) were also higher expressed in AhRR$^{-/-}$ vs WT FLiM cells (Figure 2B, S2A, Supplementary Table 1 (GSEA)). Pathways influencing the TNF and interferon response were negatively enriched in AhRR$^{-/-}$ FLiM cells, alongside genes associated with adipogenesis and lipoprotein metabolism (*Apoc1, Apoc4*) and lipid storage (*Plin2, Abca1*) (Figure 2B,

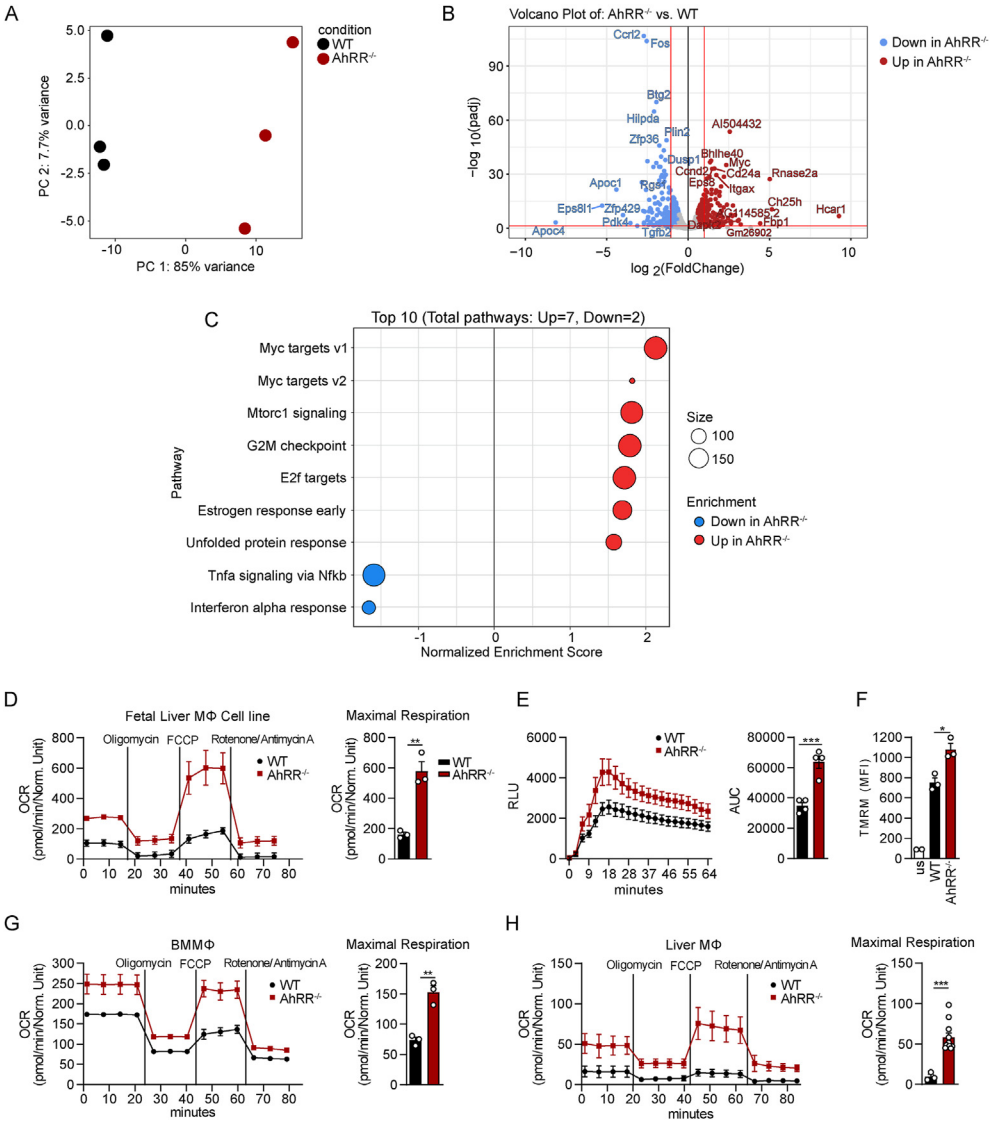

Figure 2: AhRR-deficient macrophages display an altered metabolic and gene expression profile. (**A**) Principal Component Analysis (PCA) plot depicting relationship of all samples based on dynamic gene expression of all genes comparing WT and AhRR$^{-/-}$ Fetal Liver MΦ (FLiM) cells (n = 3) and (**B**) Volcano plot depicting fold changes (FC) and FDR-adjusted p values comparing WT and AhRR$^{-/-}$ FLiM cells. Differentially expressed up- (red) and downregulated genes (blue) are shown and selected genes are highlighted. (**C**) GSEA results based on the ranked gene list between AhRR$^{-/-}$ vs WT FLiM cells, n = 3. Only significant enriched terms are visualized by the Normalized enrichment scores (NES) and the enriched terms based on the Hallmark DB, n = 3. (**D**) Mitochondrial stress test analysis of FLiM cells of WT and AhRR$^{-/-}$ mice using a Seahorse XFe96 analyzer. Oxygen consumption rate (OCR) over time (left panel) and quantification of the maximal OCR (right panel); n = 3. (**E**) ROS production of FLiM cells after stimulation with zymosan over time (left panel) and quantification depicted as area under curve (AUC, right panel); n = 4. (**F**) Flow cytometric measurement of mitochondrial membrane potential using Tetramethylrhodamine Methyl Ester (TMRM), depicted as MFI; n = 3 (WT, AhRR$^{-/-}$). us = unstained control, n = 2. (**G**) Mitochondrial stress test analysis in bone marrow-derived macrophages (BMMΦ) and (**H**) primary liver macrophages of WT and AhRR$^{-/-}$ mice. OCR over time (left panel) and quantification of the maximal OCR (right panel); For (G), n = 3 and for (H), n = 3 (WT), n = 10 (AhRR$^{-/-}$). Seahorse and ROS data show mean ± s.e.m. of at least three technical replicates from one representative experiment. At least three biologically independent experiments were performed for all OCR and ROS measurements. *p < 0.05, **p ≤ 0.01, ***p ≤ 0.001. Significance was determined using unpaired two-tailed t-tests.

S2A). These findings highlight the involvement of the AhR/AhRR signaling axis in metabolic processes on a cellular level, regulating key cellular programs such as protein synthesis and immunometabolism. To directly assess the role of AhRR in immunometabolism and mitochondrial function, WT and AhRR-deficient FLiM cells were analyzed in a Seahorse Mitochondrial Stress test. The cellular metabolic state of macrophages is linked to their activation state. Alternatively activated macrophages are often characterized by an enhanced oxidative metabolism, whereas classically activated macrophages rely on glycolysis [78]. Here, we could show that AhRR-deficient FLiM cells had higher basal and maximal respiration rates than WT FLiM cells, implying that lack of AhRR expression shifts macrophages towards alternative activation (Figure 2D, S2B). Enhanced oxidative metabolism can lead to an increase in reactive oxygen species (ROS) generation as a side product of the electron transport chain. Recent data implied that intestinal IELs of AhRR$^{-/-}$ mice showed increased intracellular ROS [36]. In accordance with these results, AhRR$^{-/-}$ FLiM cells also had elevated ROS levels after stimulation with Zymosan (Figure 2E). In line, analysis of the mitochondrial membrane potential using Tetramethylrhodamine (TMRM) staining showed a higher accumulation of the dye in mitochondria of

AhRR$^{-/-}$ cells, implying enhanced mitochondrial activity in AhRR-deficient FLiM cells (Figure 2F, S2C). Additionally, we analyzed bone marrow-derived macrophages (BMMΦ) and primary liver macrophages from WT and AhRR$^{-/-}$ mice. In line with the results shown for FLiM cells, AhRR-deficient BMMΦ and primary macrophages isolated from the liver exhibited an enhanced maximal and basal respiration rate (Figure 2G–H, S2D-E). Altogether, these data show that AhRR-deficient macrophages have an altered immunometabolic phenotype with increased mitochondrial capacity, leading to enhanced oxidative phosphorylation and ROS production.

3.3. Mice lacking AhRR solely in myeloid cells do not phenocopy global AhRR-deficient mice but show reduced diet-induced hepatosteatosis

Following these results, we hypothesized that myeloid cells, known to influence the metabolism of hepatocytes [43–45] and adipocytes [46–48] via cellular cross-talk, could be responsible for the reduced weight gain and reduced liver steatosis observed in global AhRR-deficient mice. To directly address this question, we generated AhRR$^{fl/fl}$ mice (Fig. S3A) and crossed them with LysM^{Cre} mice [53] to generate mice deficient for AhRR in myeloid cells. Deletion efficiency in macrophages was proven via qPCR (Fig. S3B). Different from our original hypothesis, after challenging AhRR$^{fl/fl}$LysM^{Cre} mice with HFD for 14 weeks, we did not observe differences in either body weight or fat mass compared to Cre-negative controls, although moderately lower glucose levels could be detected in blood (Figure 3A–C). Moreover, and in contrast to AhRR$^{-/-}$ mice, AhRR$^{fl/fl}$LysM^{Cre} mice had decreased oxygen consumption at 23 °C (Figure 3D). In line with these results, no differences in weight, morphology or adipogenic and pro-fibrotic markers were observed in the WATg (Fig. S4A-D). Nevertheless, mRNA levels of the gene encoding fatty acid synthase (*Fasn*), linked to visceral adipose tissue accumulation, along with mRNA levels of monocyte chemoattractant protein-1 (*Mcp1*) were significantly decreased in AhRR$^{fl/fl}$LysM^{Cre} mice compared to AhRR$^{fl/fl}$ control mice (Fig. S4C, E). In addition, in the HFD-fed groups, the liver weight was significantly lower (−20.86%) in AhRR$^{fl/fl}$LysM^{Cre} mice compared to control HFD mice (Figure 3E). Histological analysis revealed reduced steatosis and lower expression levels of the fatty acid binding protein 4 (*Fabp4*), commonly associated with metabolic-associated fatty liver disease (MAFLD) [79] (Figure 3F–G). Similarly, the more moderate occurrence of fibrosis assessed by Sirius Red staining and reduced expression of the pro-fibrotic marker *Col1a1* (Figure 3H–I) indicated a

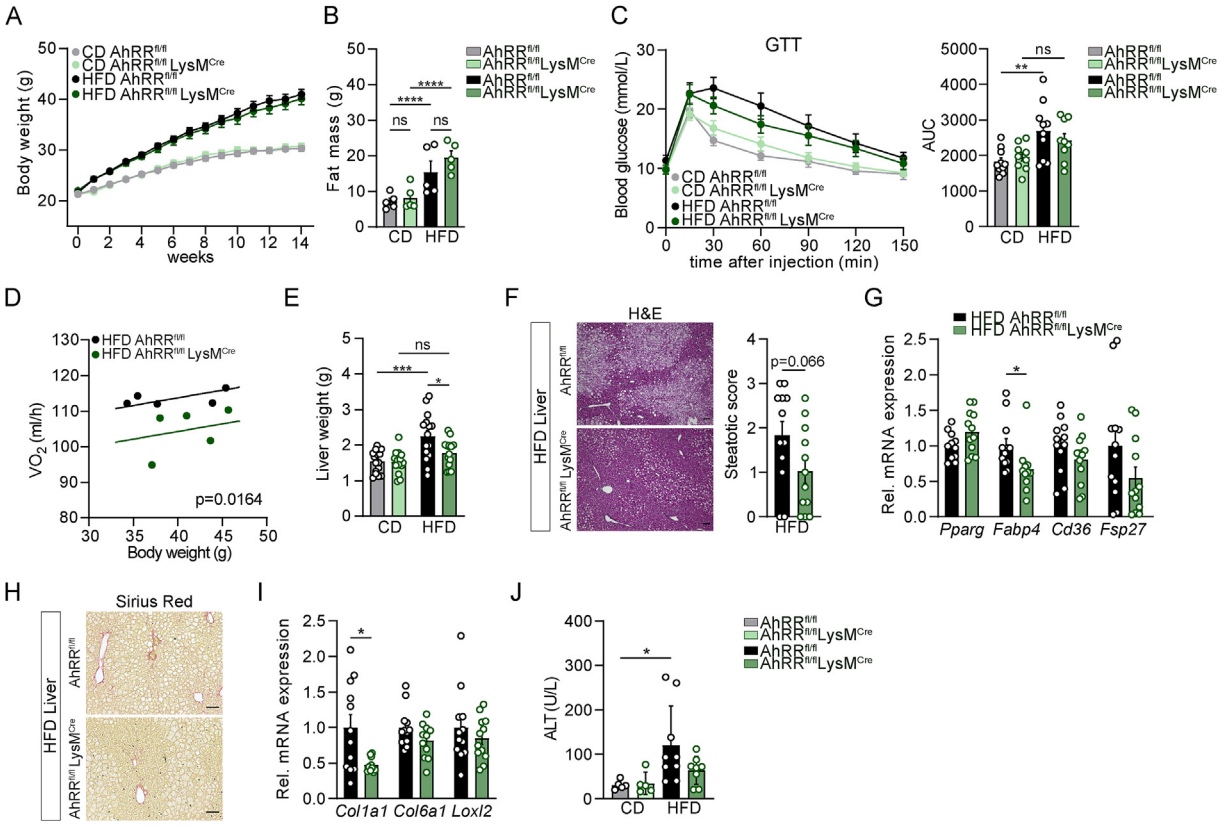

Figure 3: Lack of AhRR in myeloid cells protects from diet-induced liver steatosis. (**A-J**) WT (AhRR$^{fl/fl}$) mice and mice lacking AhRR in myeloid cells (AhRR$^{fl/fl}$LysM^{Cre}) were fed either a CD or a HFD over the course of 14 weeks. (**A**) Body weight; n = 16 (CD AhRR$^{fl/fl}$), n = 14 (CD AhRR$^{fl/fl}$LysM^{Cre}) and n = 15 (HFD AhRR$^{fl/fl}$, HFD AhRR$^{fl/fl}$LysM^{Cre}). (**B**) Total body fat mass assessed by NMR; n = 5. (**C**) Blood glucose over the course of 150 min (left) and AUC quantification (right); n = 10 (AhRR$^{fl/fl}$), n = 9 (AhRR$^{fl/fl}$LysM^{Cre}). (**D**) ANCOVA of oxygen consumption rate of HFD mice; n = 5 for all groups. (**E**) Liver weight, n = 16 (CD AhRR$^{fl/fl}$), n = 15 (HFD AhRR$^{fl/fl}$), n = 14 (CD AhRR$^{fl/fl}$LysM^{Cre}, HFD AhRR$^{fl/fl}$LysM^{Cre}). (**F**) Representative H&E (left panel) and semiquantitative analysis of the steatotic score (right panel) of HFD liver samples. Scale bars, 100 μm; n = 12 for both groups. (**G**) Relative mRNA expression levels of lipid-related markers in HFD liver samples, n = 12 for all groups. (**H**) Representative Sirius Red staining of HFD liver samples. Scale bars, 100 μm, n = 12 for all groups. (**I**) Relative mRNA expression of pro-fibrotic markers in HFD liver samples; n = 12 for all groups. (**J**) ALT concentration in plasma of AhRR$^{fl/fl}$ and AhRR$^{fl/fl}$LysM^{Cre} mice fed either CD or HFD for 14 weeks; n = 5 (CD AhRR$^{fl/fl}$, CD AhRR$^{fl/fl}$LysM^{Cre}), n = 9 (HFD AhRR$^{fl/fl}$), and n = 8 (HFD AhRR$^{fl/fl}$LysM^{Cre}). *p < 0.05, **p ≤ 0.01, ***p ≤ 0.001. Significance was determined using unpaired two-tailed t-tests (F, G, and I) and one-way ANOVA with Tukey's multiple-comparison test (B, C, E and J). Data are mean ± s.e.m.

reduced fatty liver disease in AhRR$^{fl/fl}$LysM^{Cre} mice compared to AhRR$^{fl/fl}$ HFD-fed mice. To further corroborate these findings, we analyzed the levels of plasma ALT after HFD feeding. ALT levels were significantly increased in AhRR$^{fl/fl}$ control mice, whereas they remained unchanged in AhRR$^{fl/fl}$LysM^{Cre} mice upon HFD feeding (Figure 3J). Altogether, these data demonstrate that the lack of AhRR in myeloid cells does not ameliorate DIO but protects from severe diet-induced hepatosteatosis and slows down progression of liver disease.

3.4. Lack of AhR in myeloid cells aggravates diet-induced hepatosteatosis and fibrosis

Next, we analyzed if the protective effects seen in AhRR$^{fl/fl}$LysM^{Cre} mice could be recapitulated in AhR$^{fl/fl}$LysM^{Cre} mice, as global deficiency of both, AhRR and AhR conferred protection from DIO and MAFLD. Remarkably, like AhRR$^{fl/fl}$LysM^{Cre} mice, AhR$^{fl/fl}$LysM^{Cre} mice were not protected from diet-induced weight gain following 14 weeks of HFD feeding (Figure 4A). In line with these results, no differences in WATg weight, expression of adipogenic markers (*Fabp4, Pparg, Adipoq, Cd36, and Fasn*), and serum cholesterol levels were observed (Figure 4B–D). Strikingly, histological analysis of WATg revealed a high accumulation of F4/80-positive cells in AhR$^{fl/fl}$LysM^{Cre} mice compared to AhR$^{fl/fl}$ mice (Figure 4E). Similarly, AhR$^{fl/fl}$LysM^{Cre} mice showed increased collagen deposition, accompanied with a significantly higher fibrosis score and increased *Col1a1* and *Col6a1* mRNA levels (Figure 4F–G). In line with these results, histological analysis showed increased hepatosteatosis, whereas the liver weight was not changed (Figure 4H–I). Although *Pparg* levels were significantly decreased, its direct target *Fsp27*, which prevents lipid mobilization and promotes intracellular lipid storage [80], was increased by 81.5% on average (Figure 4J). Moreover, the liver of AhR$^{fl/fl}$LysM^{Cre} mice appeared more fibrotic and depicted increased *Col1a1* and *Col6a1* mRNA expression levels (Figure 4K). In line, we observed a significant increase in serum ALT levels (Figure 4L). Altogether these data indicate that loss of AhR in myeloid cells severely affects the consequences of DIO accelerating the progression of MAFLD and aggravating visceral adipose tissue fibrosis.

4. DISCUSSION

In the last decades, obesity has become one of the leading risk factors associated with poor cardiometabolic health, diabetes, dyslipidemia, and cancer [81,82]. It is known that the AhR links recognition of

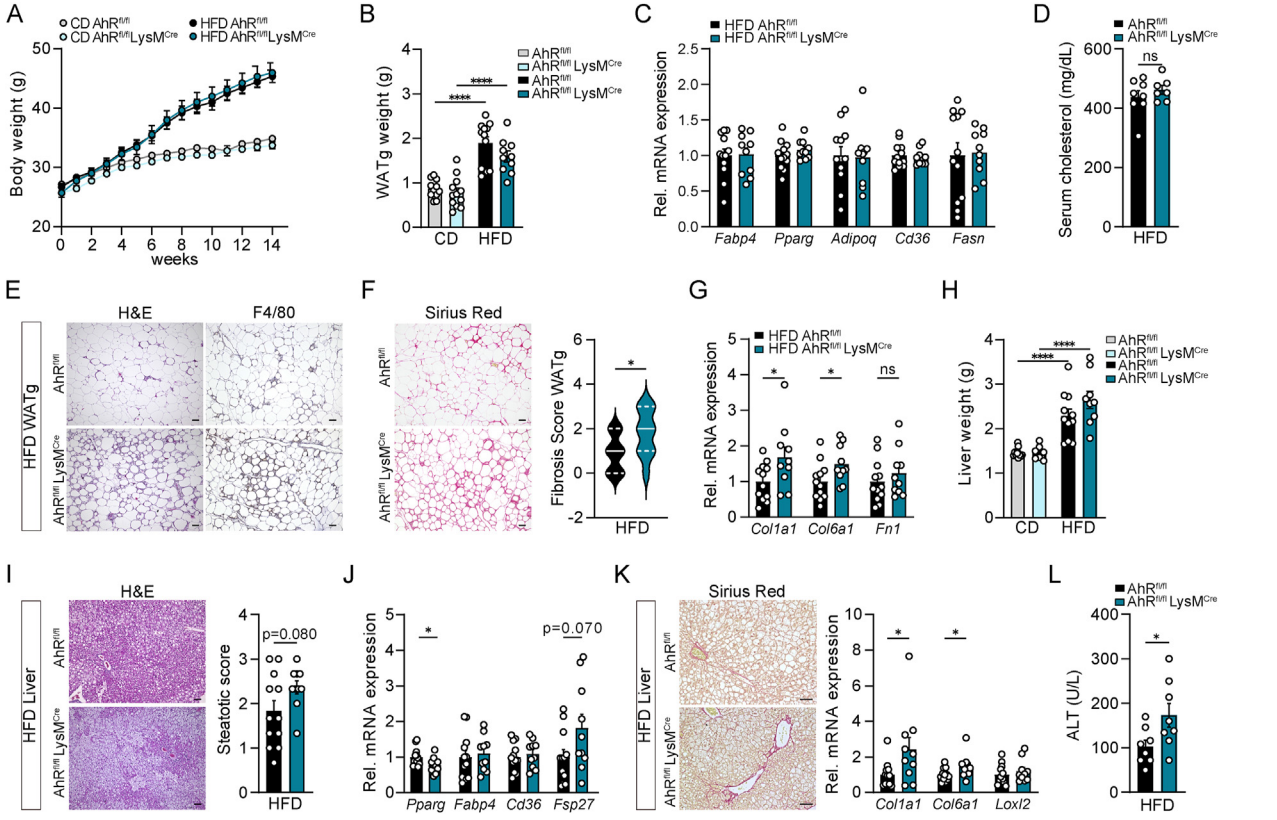

Figure 4: Lack of AhR in myeloid cells aggravates hepatic steatosis and induces fibrosis in liver and adipose tissue. (**A-L**) WT (AhR$^{fl/fl}$) mice and mice lacking AhR in myeloid cells (AhR$^{fl/fl}$LysM^{Cre}) were fed either a CD or a HFD over the course of 14 weeks. For all experiments n = 11 (CD AhR$^{fl/fl}$), n = 12 (CD AhR$^{fl/fl}$LysM^{Cre}), n = 12 (HFD AhR$^{fl/fl}$), and n = 10 (HFD AhR$^{fl/fl}$LysM^{Cre}) unless otherwise stated in the figure legends. (**A**) Body weight. (**B**) WATg weight in grams. (**C**) Relative mRNA levels of adipogenic markers in WATg of HFD mice. (**D**) Total serum cholesterol; n = 8 (AhR$^{fl/fl}$) and n = 7 (AhR$^{fl/fl}$LysM^{Cre}). (**E**) Representative H&E (left panel) and F4/80 (right panel) staining of the WATg of HFD mice. Scale bars, 100 μm. n = 11 (AhR$^{fl/fl}$) and n = 10 (AhR$^{fl/fl}$LysM^{Cre}). (**F**) Representative Sirius Red staining (left panel) and semiquantitative analysis of the fibrosis score (right panel) of the WATg of HFD mice. Scale bars, 100 μm; n = 11 (AhR$^{fl/fl}$) and n = 10 (AhR$^{fl/fl}$LysM^{Cre}). (**G**) Relative mRNA levels of pro-fibrotic markers in WATg of HFD mice. (**H**) Liver weight. (**I**) Representative H&E stainings (left panel) and semiquantitative analysis of the steatotic score (right panel) of HFD liver samples. Scale bars, 100 μm. (**J**) Relative mRNA expression levels of lipid-related markers in the liver of HFD mice. (**K**) Representative Sirius Red staining of liver sections. Scale bars, 100 μm (left panel). Right, relative mRNA expression levels of pro-fibrotic markers in the liver of HFD mice. (**L**) Serum ALT concentration of AhR$^{fl/fl}$ and AhR$^{fl/fl}$LysM^{Cre} mice fed a HFD for 14 weeks; n = 8 for both groups. *p < 0.05, **p ≤ 0.01, ***p ≤ 0.001. Significance was determined using unpaired two-tailed t-tests (C, D, F, G, I, J, K, and L) and one-way ANOVA with Tukey's multiple-comparison test (B and H). Data are mean ± s.e.m.

environmental stimuli to the homeostasis of metabolic organs [83,84] as well as overall metabolic health and development of obesity [19,72]. In addition, global AhR deficiency can protect mice from DIO associated with ameliorated hepatic steatosis and increased energy expenditure [8,19]. Here, we analyzed the influence of the AhRR on the development of DIO and liver damage. We previously described that AhRR expression is mainly detected in hematopoietic cells of barrier organs and their draining lymph nodes [32] but the role of the AhRR in macrophage programming and its influence on metabolic diseases was still unclear. Unexpectedly, global deficiency of the AhRR protected mice from DIO, similar to the effects observed in $AhR^{-/-}$ mice. This was accompanied by an increase in whole-body energy expenditure and diminished hepatosteatosis, thereby identifying AhRR as a potential regulator of metabolic health. Alongside improved glucose tolerance and insulin sensitivity, $AhRR^{-/-}$ mice showed decreased body weight and fat mass. As we observed a reduced size of adipocytes in WATg of global $AhRR^{-/-}$ mice, it cannot be excluded that the AhRR to some extent also controls adipocyte metabolism directly. More likely, however, a cross-talk of several cell types, in particular immune cells and non-hematopoietic parenchymal or stromal cells accounts for the ameliorated DIO in global $AhRR^{-/-}$ mice.

A possible explanation for the finding that AhR- and AhRR-deficient mice show a similar phenotype regarding the development of DIO is the differential regulation and a stronger cell type-specific expression of the AhRR compared to AhR. A similar scenario has been observed in the context of dextran sodium sulfate (DSS)-induced intestinal inflammation where AhR- as well as AhRR deficiency aggravated susceptibility to inflammatory bowel disease. In the intestine, the AhRR is expressed in various immune cell subtypes but not in epithelial cells, whereas AhR expression is of particular importance in intestinal epithelial cells controlling the expression of CYP enzymes [32,85,86]. Thus, we hypothesize that AhRR deficiency ameliorates DIO because of enhanced AhR activity in certain cell types [32], an effect that may also be achieved by higher ligand availability. In line, Choi et al. showed that dietary supplementation of the AhR ligand precursor I3C regulated adipogenic and thermogenic gene programs such that DIO was reduced [73]. We confirmed this effect of decreased weight gain and ameliorated hepatosteatosis in WT mice fed I3C-supplemented HFD but observed no further reduction in weight gain and steatosis by I3C in AhRR-deficient mice. Thus, AhRR deficiency has a stronger effect than I3C supplementation.

Macrophages, which are key regulators of tissue homeostasis and repair, express the AhRR [32]. Previous studies showed that macrophage metabolism influences their phenotype and plasticity to adapt to different environments in health and disease, thus enabling specific effector functions [87]. Therefore, we assessed how AhRR deficiency affects cellular programming in macrophages. Here, we observed increased oxidative phosphorylation in conjunction with higher mitochondrial membrane potential in AhRR-deficient macrophages, indicating an overall enhanced mitochondrial activity. Interestingly, the AhR signaling pathway has been identified as a regulator of mitochondrial homeostasis in the liver [88]. ROS are generated as a side product of oxidative phosphorylation in the mitochondrial electron transport chain [89] or as a result of CYP enzymatic activity [90], which is enhanced in the absence of the AhRR. In accordance with the study by Panda et al., reporting an increased ROS production in AhRR-deficient IELs [36], we detected elevated macrophage ROS production and alterations in the level of plasma TCA cycle intermediates after HFD feeding. In line with alterations in mitochondrial metabolism, transcriptomic analysis of FLiM cells revealed an enrichment of Myc and mTORC1 pathways known to regulate mitochondrial biogenesis and function besides other cellular processes [91,92]. Altogether, our data underline the importance of AhRR in regulating mitochondrial activity.

Further, genes associated with *de novo* lipogenesis, such as *Acly* encoding ATP citrate lyase and *Acaca* encoding Acetyl-CoA carboxylase, both essential for fatty acid synthesis, were enriched in AhRR-deficient FLiM cells. It has been shown that changes in *Acaca* affect the bioenergetic profile of macrophages and influence their response to pro-inflammatory stimuli [93]. Moreover, *Acly* expression is associated with increased ROS and prostaglandin E2 production and has been suggested to increase phagocytosis in TLR-activated BMMΦ [94]. Wculek et al. revealed that macrophages with high demand for lipid handling rely on mitochondrial respiration to meet their metabolic need [95]. Thus, the OXPHOS capacity of macrophages directly correlates with their functional capacity to handle high lipid burden. Consequently, we hypothesize that in the absence of AhRR expression, the overall enhanced expression of *de novo* lipogenesis genes and increased mitochondrial activity contribute to alternative activation and elevated macrophage ROS levels.

Despite the observed alterations in metabolic programming of AhRR-deficient macrophages, analysis of mice with a conditional loss of AhRR in myeloid cells only partially recapitulated the phenotype of global AhRR-deficient mice in the DIO model. Thus, $AhRR^{fl/fl}LysM^{Cre}$ mice were not protected from developing DIO and metabolic syndrome but showed protection from severe hepatosteatosis and obesity-associated liver injury. In contrast, $AhR^{fl/fl}LysM^{Cre}$ mice revealed an exacerbation of liver disease following 14 weeks of HFD. It was shown before that Kupffer cells, liver-resident macrophages, interact with hepatocytes and thereby shape the tissue environment, regulating hepatic lipid metabolism and the liver's response to HFD [43,96,97]. Moreover, macrophages in the liver are key players in MAFLD development and are responsible for the efferocytosis of lipid-laden hepatocytes [45,98]. Thus, through deletion of the AhRR in myeloid cells, the progression of MAFLD was slowed down, although the mice still exhibited signs of metabolic syndrome. It should be noted that besides macrophages, neutrophils are also affected by $LysM^{Cre}$-mediated deletion [53]. As granulocytes do not express *Ahr* nor *Ahrr* [99], it is unlikely, however, that neutrophils account for the observed phenotype. Taken together, our results suggest AhRR as a rheostat of macrophage metabolism and function conferring a more protective and lipid-tolerant status in the liver.

Liver fibrosis often occurs as a consequence of chronic liver damage and is positively correlated with higher mortality rates [100]. Interestingly, we observed a significant decrease in the expression levels of the pro-fibrotic marker *Col1a1* in the liver of HFD-fed $AhRR^{fl/fl}LysM^{Cre}$ mice. In contrast, $AhR^{fl/fl}LysM^{Cre}$ mice displayed higher expression of *Col1a1* and *Col6a1*, alongside exacerbated Sirius Red staining. The role of AhR in hepatic fibrosis, however, is controversially discussed. While global AhR-deficient mice spontaneously developed periportal liver fibrosis [101], TCDD-induced activation of the AhR has also been described to induce hepatic fibrosis [102–104]. A possible explanation for this paradox is that very high doses of dioxin, as a strong AhR agonist, can disrupt AhR signaling and thus promote fibrosis [104]. In contrast, the provision of another AhR ligand was shown to ameliorate CCl_4-induced fibrosis [105], suggesting a protective role of mild AhR activation regarding liver fibrosis. It has been reported that global AhR deficiency promotes the activation of hepatic stellate cells (HSC), key players in the development of hepatic fibrosis [105]. Liver macrophages are the main regulators of HSC function, producing pro-fibrogenic cytokines, which support survival of activated HSC [106]. Activated HSC secrete chemokines attracting macrophages, and

consequently aggravate the progression of liver fibrosis. Of note, loss of AhR expression in HSC but not in hepatocytes appeared to be responsible for the development of periportal fibrosis [105]. Similarly, macrophages are also involved in adipose tissue fibrosis, stimulating extracellular matrix (ECM) accumulation [107], but also clearing excessive ECM through collagen uptake and degradation [108]. Here we demonstrate that loss of AhR in macrophages worsens the development of HFD-induced fibrosis, while $AhRR^{fl/fl}LysM^{Cre}$ mice show reduced collagen deposition. Therefore, the expression of AhR in macrophages and the regulation of AhR signaling via AhRR both play a role in the development of diet-induced fibrosis depending on external stimuli.

Besides the differential role of AhR and AhRR in macrophages in the context of DIO and liver damage, the functional importance of the AhR strongly differs between cell types and stage of development. For example, early developmental ablation of the AhR either globally or in endothelial cells causes failure of ductus venosus closure in the liver [109] which may affect diet-induced liver damage. As a result, considering its restricted cell type-specific expression [32,36], the AhRR may represent a more promising target for potential pharmacological therapy of metabolic diseases than the AhR itself.

CREDIT AUTHORSHIP CONTRIBUTION STATEMENT

Frederike J. Graelmann: Writing — original draft, Visualization, Validation, Methodology, Investigation, Formal analysis, Data curation, Conceptualization. **Fabian Gondorf:** Methodology, Investigation, Funding acquisition, Conceptualization. **Yasmin Majlesain:** Writing — original draft, Visualization, Methodology, Investigation. **Birte Niemann:** Methodology, Investigation. **Katarina Klepac:** Investigation. **Dominic Gosejacob:** Investigation. **Marlene Gottschalk:** Investigation. **Michelle Mayer:** Investigation. **Irina Iriady:** Investigation. **Philip Hatzfeld:** Investigation. **Sophie K. Lindenberg:** Investigation. **Klaus Wunderling:** Methodology, Investigation. **Christoph Thiele:** Resources. **Zeinab Abdullah:** Resources, Methodology. **Wei He:** Methodology, Investigation. **Karsten Hiller:** Validation, Resources, Methodology, Funding acquisition. **Kristian Händler:** Investigation. **Marc D. Beyer:** Resources. **Thomas Ulas:** Software, Methodology, Formal analysis, Data curation. **Alexander Pfeifer:** Supervision, Resources, Funding acquisition, Conceptualization. **Charlotte Esser:** Validation, Supervision, Resources, Funding acquisition, Conceptualization. **Heike Weighardt:** Writing — review & editing, Writing — original draft, Visualization, Validation, Supervision, Resources, Methodology, Funding acquisition, Conceptualization. **Irmgard Förster:** Writing — review & editing, Writing — original draft, Supervision, Resources, Funding acquisition, Conceptualization. **Laia Reverte-Salisa:** Writing — review & editing, Writing — original draft, Visualization, Validation, Supervision, Methodology, Investigation, Formal analysis, Data curation, Conceptualization.

ACKNOWLEDGEMENTS

We are grateful to Babette Martiensen for technical help. This work was supported by the Deutsche Forschungsgemeinschaft (DFG, German Research Foundation) through SFB 1454 (Project No. 432325352) (to I.F., K.H., M.D.B., A.*P. and* C.T.), EXC 1023 (Project No. 194445620) (to I.F.), EXC 2151 (Project No. 390873048) (to I.F.), WE 2625/4-1 (to H.W.), and TRR 333/1—450149205 (to I.F. and A.P.); the University of Bonn through an Argelander grant to F.G., as well as the Jürgen Manchot Foundation (to I.F. and H.W.).

Illustrations in the graphical abstract were created with Biorender.com.

DECLARATION OF COMPETING INTEREST

The authors declare that they have no known competing financial interests or personal relationships that could have appeared to influence the work reported in this paper.

DATA AVAILABILITY

Data will be made available on request.

APPENDIX A. SUPPLEMENTARY DATA

Supplementary data to this article can be found online at https://doi.org/10.1016/j.molmet.2024.101963.

REFERENCES

[1] Stockinger B, Shah K, Wincent E. AHR in the intestinal microenvironment: safeguarding barrier function. Nat Rev Gastroenterol Hepatol 2021:559—70. https://doi.org/10.1038/s41575-021-00430-8.

[2] Rothhammer V, Quintana FJ. The aryl hydrocarbon receptor: an environmental sensor integrating immune responses in health and disease. Nat Rev Immunol 2019;19(3):184—97. https://doi.org/10.1038/s41577-019-0125-8.

[3] Denison MS, Soshilov AA, He G, Degroot DE, Zhao B. Exactly the same but different: promiscuity and diversity in the molecular mechanisms of action of the aryl hydrocarbon (dioxin) receptor. Toxicol Sci 2011;124(1):1—22. https://doi.org/10.1093/toxsci/kfr218.

[4] Schiering C, Wincent E, Metidji A, Iseppon A, Li Y, Potocnik AJ, et al. Feedback control of AHR signalling regulates intestinal immunity. Nature 2017;542(7640):242—5. https://doi.org/10.1038/nature21080.

[5] Diny NL, Schonfeldova B, Shapiro M, Winder ML, Varsani-Brown S, Stockinger B. The aryl hydrocarbon receptor contributes to tissue adaptation of intestinal eosinophils in mice. J Exp Med 2022;219(4). https://doi.org/10.1084/jem.20210970.

[6] Qiu J, Heller JJ, Guo X, Chen ZE, Fish K, Fu Y-X, et al. The aryl hydrocarbon receptor regulates gut immunity through modulation of innate lymphoid cells. Immunity 2012;36(1):92—104. https://doi.org/10.1016/j.immuni.2011.11.011.

[7] Jaeger C, Tischkau SA. Role of aryl hydrocarbon receptor in circadian clock disruption and metabolic dysfunction. Environ Health Insights 2016. https://doi.org/10.4137/EHI.S38343.

[8] Kerley-Hamilton JS, Trask HW, Ridley CJA, Dufour E, Ringelberg CS, Nurinova N, et al. Obesity is mediated by differential aryl hydrocarbon receptor signaling in mice fed a western diet. Environ Health Perspect 2012;120(9):1252—9. https://doi.org/10.1289/ehp.1205003.

[9] Natividad JM, Agus A, Planchais J, Lamas B, Jarry AC, Martin R, et al. Impaired aryl hydrocarbon receptor ligand production by the gut microbiota is a key factor in metabolic syndrome. Cell Metabol 2018;28(5):737—49. https://doi.org/10.1016/j.cmet.2018.07.001.

[10] Fader KA, Nault R, Kirby MP, Markous G, Matthews J, Zacharewski TR. Convergence of hepcidin deficiency, systemic iron overloading, heme accumulation, and REV-ERBα/β activation in aryl hydrocarbon receptor-elicited hepatotoxicity. Toxicol Appl Pharmacol 2017;321:1—17. https://doi.org/10.1016/j.taap.2017.02.006.

[11] Boverhof DR, Burgoon LD, Tashiro C, Sharratt B, Chittim B, Harkema JR, et al. Comparative toxicogenomic analysis of the hepatotoxic effects of TCDD in Sprague Dawley rats and C57BL/6 mice. Toxicol Sci 2006;94(2):398—416. https://doi.org/10.1093/toxsci/kfl100.

[12] Lee JH, Wada T, Febbraio M, He J, Matsubara T, Lee MJ, et al. A novel role for the dioxin receptor in fatty acid metabolism and hepatic steatosis.

Gastroenterology 2010;139(2):653–63. https://doi.org/10.1053/j.gastro.2010.03.033.
[13] Lindén J, Lensu S, Tuomisto J, Pohjanvirta R. Dioxins, the aryl hydrocarbon receptor and the central regulation of energy balance. Front Neuroendocrinol 2010:452–78. https://doi.org/10.1016/j.yfrne.2010.07.002.
[14] Hutin D, Tamblyn L, Gomez A, Grimaldi G, Soedling H, Cho T, et al. Hepatocyte-specific deletion of TIPARP, a negative regulator of the aryl hydrocarbon receptor, is sufficient to increase sensitivity to dioxin-induced wasting syndrome. Toxicol Sci 2018;165(2):347–60. https://doi.org/10.1093/toxsci/kfy136.
[15] Baker NA, Shoemaker R, English V, Larian N, Sunkara M, Morris AJ, et al. Effects of adipocyte aryl hydrocarbon receptor deficiency on PCB-induced disruption of glucose homeostasis in lean and obese mice. Environ Health Perspect 2015;123(10):944–50. https://doi.org/10.1289/ehp.1408594.
[16] Brulport A, Le Corre L, Chagnon MC. Chronic exposure of 2,3,7,8-tetrachlorodibenzo-p-dioxin (TCDD) induces an obesogenic effect in C57BL/6J mice fed a high fat diet. Toxicology 2017;390:43–52. https://doi.org/10.1016/j.tox.2017.07.017.
[17] Jin Y, Miao W, Lin X, Wu T, Shen H, Chen S, et al. Sub-chronically exposing mice to a polycyclic aromatic hydrocarbon increases lipid accumulation in their livers. Environ Toxicol Pharmacol 2014;38(2):353–63. https://doi.org/10.1016/j.etap.2014.07.014.
[18] Park WH, Jun DW, Kim JT, Jeong JH, Park H, Chang YS, et al. Novel cell-based assay reveals associations of circulating serum AhR-ligands with metabolic syndrome and mitochondrial dysfunction. Biofactors 2013;39(4):494–504. https://doi.org/10.1002/biof.1092.
[19] Xu CX, Wang C, Zhang ZM, Jaeger CD, Krager SL, Bottum KM, et al. Aryl hydrocarbon receptor deficiency protects mice from diet-induced adiposity and metabolic disorders through increased energy expenditure. Int J Obes 2015;39(8):1300–9. https://doi.org/10.1038/ijo.2015.63.
[20] Girer N, Carter D, Bhattarai N, Mustafa M, Denner L, Porter C, et al. Inducible loss of the aryl hydrocarbon receptor activates perigonadal white fat respiration and Brown fat thermogenesis via fibroblast growth factor 21. Int J Mol Sci 2019;20(4):950. https://doi.org/10.3390/ijms20040950.
[21] Haque N, Ojo ES, Krager SL, Tischkau SA. Deficiency of adipose aryl hydrocarbon receptor protects against diet-induced metabolic dysfunction through sexually dimorphic mechanisms. Cells 2023;12(13). https://doi.org/10.3390/cells12131748.
[22] Lu P, Yan J, Liu K, Garbacz WG, Wang P, Xu M, et al. Activation of aryl hydrocarbon receptor dissociates fatty liver from insulin resistance by inducing fibroblast growth factor 21. Hepatology 2015;61(6):1908–19. https://doi.org/10.1002/hep.27719.
[23] Angrish MM, Jones AD, Harkema JR, Zacharewski TR. Aryl hydrocarbon receptor-mediated induction of stearoyl-coa Desaturase 1 alters hepatic fatty acid composition in TCDD-elicited steatosis. Toxicol Sci 2011;124(2):299–310. https://doi.org/10.1093/toxsci/kfr226.
[24] Tanos R, Murray IA, Smith PB, Patterson A, Perdew GH. Role of the Ah receptor in homeostatic control of fatty acid synthesis in the liver. Toxicol Sci 2012;129(2):372–9. https://doi.org/10.1093/toxsci/kfs204.
[25] Gutiérrez-Vázquez C, Quintana FJ. Regulation of the immune response by the aryl hydrocarbon receptor. Immunity 2018:19–33. https://doi.org/10.1016/j.immuni.2017.12.012.
[26] Stockinger B, Meglio P Di, Gialitakis M, Duarte JH. The aryl hydrocarbon receptor: multitasking in the immune system. Annu Rev Immunol 2014;32(1):403–32. https://doi.org/10.1146/annurev-immunol-032713-120245.
[27] Wincent E, Bengtsson J, Bardbori AM, Alsberg T, Luecke S, Rannug U, et al. Inhibition of cytochrome P4501-dependent clearance of the endogenous agonist FICZ as a mechanism for activation of the aryl hydrocarbon receptor. Proc Natl Acad Sci USA 2012;109(12):4479–84. https://doi.org/10.1073/pnas.1118467109.
[28] Wincent E, Kubota A, Timme-Laragy A, Jönsson ME, Hahn ME, Stegeman JJ. Biological effects of 6-formylindolo[3,2-b]carbazole (FICZ) in vivo are enhanced by loss of CYP1A function in an Ahr2-dependent manner. Biochem Pharmacol 2016;110–111:117–29. https://doi.org/10.1016/j.bcp.2016.04.012.
[29] MacPherson L, Ahmed S, Tamblyn L, Krutmann J, Förster I, Weighardt H, et al. Aryl hydrocarbon receptor repressor and TiPARP (ARTD14) use similar, but also distinct mechanisms to repress aryl hydrocarbon receptor signaling. Int J Mol Sci 2014;15(5):7939–57. https://doi.org/10.3390/ijms15057939.
[30] Mimura J, Ema M, Sogawa K, Fujii-Kuriyama Y. Identification of a novel mechanism of regulation of Ah (dioxin) receptor function. Gene Dev 1999;13(1):20–5. https://doi.org/10.1101/gad.13.1.20.
[31] Vogel CFA, Haarmann-Stemmann T. The aryl hydrocarbon receptor repressor – more than a simple feedback inhibitor of AhR signaling: clues for its role in inflammation and cancer. Curr Opin Toxicol 2017;1:109–19. https://doi.org/10.1016/j.cotox.2017.02.004.
[32] Brandstätter O, Schanz O, Vorac J, König J, Mori T, Maruyama T, et al. Balancing intestinal and systemic inflammation through cell type-specific expression of the aryl hydrocarbon receptor repressor. Sci Rep 2016;6(December 2015):26091. https://doi.org/10.1038/srep26091.
[33] Ahmed S, Bott D, Gomez A, Tamblyn L, Rasheed A, Cho T, et al. Loss of the mono-ADP-ribosyltransferase, tiparp, increases sensitivity to dioxin-induced steatohepatitis and lethality. J Biol Chem 2015;290(27):16824–40. https://doi.org/10.1074/jbc.M115.660100.
[34] Hosoya T, Harada N, Mimura J, Motohashi H, Takahashi S, Nakajima O, et al. Inducibility of cytochrome P450 1A1 and chemical carcinogenesis by benzo[a]pyrene in AhR repressor-deficient mice. Biochem Biophys Res Commun 2008;365(3):562–7. https://doi.org/10.1016/j.bbrc.2007.11.016.
[35] Tigges J, Weighardt H, Wolff S, Götz C, Förster I, Kohne Z, et al. Aryl hydrocarbon receptor repressor (AhRR) function revisited: repression of CYP1 activity in human skin fibroblasts is not related to AhRR expression. J Invest Dermatol 2013;133(1):87–96. https://doi.org/10.1038/jid.2012.259.
[36] Panda SK, Peng V, Sudan R, Ulezko Antonova A, Di Luccia B, Ohara TE, et al. Repression of the aryl-hydrocarbon receptor prevents oxidative stress and ferroptosis of intestinal intraepithelial lymphocytes. Immunity 2023. https://doi.org/10.1016/j.immuni.2023.01.023.
[37] Brestoff JR, Wilen CB, Moley JR, Li Y, Zou W, Malvin NP, et al. Intercellular mitochondria transfer to macrophages regulates white adipose tissue homeostasis and is impaired in obesity. Cell Metabol 2021;33(2):270–282.e8. https://doi.org/10.1016/j.cmet.2020.11.008.
[38] Rosina M, Ceci V, Turchi R, Chuan L, Borcherding N, Sciarretta F, et al. Ejection of damaged mitochondria and their removal by macrophages ensure efficient thermogenesis in brown adipose tissue. Cell Metabol 2022;34(4):533–548.e12. https://doi.org/10.1016/j.cmet.2022.02.016.
[39] Feuerer M, Herrero L, Cipolletta D, Naaz A, Wong J, Nayer A, et al. Lean, but not obese, fat is enriched for a unique population of regulatory T cells that affect metabolic parameters. Nat Med 2009;15(8):930–9. https://doi.org/10.1038/nm.2002.
[40] Lee MW, Odegaard JI, Mukundan L, Qiu Y, Molofsky AB, Nussbaum JC, et al. Activated type 2 innate lymphoid cells regulate beige fat biogenesis. Cell 2015;160(1–2):74–87. https://doi.org/10.1016/j.cell.2014.12.011.
[41] Nguyen KD, Qiu Y, Cui X, Goh YPS, Mwangi J, David T, et al. Alternatively activated macrophages produce catecholamines to sustain adaptive thermogenesis. Nature 2011;480(7375):104–8. https://doi.org/10.1038/nature10653.
[42] Wolf Y, Boura-Halfon S, Cortese N, Haimon Z, Sar Shalom H, Kuperman Y, et al. Brown-adipose-tissue macrophages control tissue innervation and homeostatic energy expenditure. Nat Immunol 2017;18(6):665–74. https://doi.org/10.1038/ni.3746.

[43] Diehl KL, Vorac J, Hofmann K, Meiser P, Unterweger I, Kuerschner L, et al. Kupffer cells sense free fatty acids and regulate hepatic lipid metabolism in high-fat diet and inflammation. Cells 2020;9(10):1—16. https://doi.org/10.3390/cells9102258.

[44] Tran S, Baba I, Poupel L, Dussaud S, Moreau M, Gélineau A, et al. Impaired kupffer cell self-renewal alters the liver response to lipid overload during non-alcoholic steatohepatitis. Immunity 2020;53(3):627—640.e5. https://doi.org/10.1016/j.immuni.2020.06.003.

[45] Wang X, He Q, Zhou C, Xu Y, Liu D, Fujiwara N, et al. Prolonged hypernutrition impairs TREM2-dependent efferocytosis to license chronic liver inflammation and NASH development. Immunity 2023;56(1):58—77.e11. https://doi.org/10.1016/j.immuni.2022.11.013.

[46] Chavakis T, Alexaki VI, Ferrante AW. Macrophage function in adipose tissue homeostasis and metabolic inflammation. Nat Immunol 2023:757—66. https://doi.org/10.1038/s41590-023-01479-0.

[47] Cox N, Crozet L, Holtman IR, Loyher PL, Lazarov T, White JB, et al. Diet-regulated production of PDGFcc by macrophages controls energy storage. Science 2021;373(6550). https://doi.org/10.1126/science.abe9383.

[48] Jaitin DA, Adlung L, Thaiss CA, Weiner A, Li B, Descamps H, et al. Lipid-associated macrophages control metabolic homeostasis in a trem2-dependent manner. Cell 2019;178(3):686—698.e14. https://doi.org/10.1016/j.cell.2019.05.054.

[49] Castoldi A, De Souza CN, Saraiva Câmara NO, Moraes-Vieira PM. The macrophage switch in obesity development. Front Immunol 2016. https://doi.org/10.3389/fimmu.2015.00637.

[50] Schmidt JV, Su GH, Reddy JK, Simon MC, Bradfield CA. Characterization of a murine Ahr null allele: involvement of the Ah receptor in hepatic growth and development. Proc Natl Acad Sci USA 1996;93(13):6731—6. https://doi.org/10.1073/pnas.93.13.6731.

[51] Haarmann-Stemmann T, Abel J. The arylhydrocarbon receptor repressor (AhRR): structure, expression, and function. Biol Chem 2006;387(9):1195—9. https://doi.org/10.1515/BC.2006.147.

[52] Baba T, Mimura J, Gradin K, Kuroiwa A, Watanabe T, Matsuda Y, et al. Structure and expression of the ah receptor repressor gene. J Biol Chem 2001;276(35):33101—10. https://doi.org/10.1074/jbc.M011497200.

[53] Clausen B, Burkhardt C, Reith W, Renkawitz R, Förster I. Conditional gene targeting in macrophage and granulocytes using LysMcre mice. Transgenic Res 1999. https://doi.org/10.1023/A.

[54] Wunderling K, Leopold C, Jamitzky I, Yaghmour M, Zink F, Kratky D, et al. Hepatic synthesis of triacylglycerols containing medium-chain fatty acids is dominated by diacylglycerol acyltransferase 1 and efficiently inhibited by etomoxir. Mol Metabol 2021;45. https://doi.org/10.1016/j.molmet.2020.101150.

[55] Fejer G, Wegner MD, Györy I, Cohen I, Engelhard P, Voronov E, et al. Non-transformed, GM-CSF-dependent macrophage lines are a unique model to study tissue macrophage functions. Proc Natl Acad Sci USA 2013;110(24). https://doi.org/10.1073/pnas.1302877110.

[56] Sethunath D, Morusu S, Tuceryan M, Cummings OW, Zhang H, Yin XM, et al. Automated assessment of steatosis in murine fatty liver. PLoS One 2018;13(5). https://doi.org/10.1371/journal.pone.0197242.

[57] Lassen PB, Charlotte F, Liu Y, Bedossa P, Le Naour G, Tordjman J, et al. The fat score, a fibrosis score of adipose tissue: predicting weight-loss outcome after gastric bypass. J Clin Endocrinol Metab 2017;102(7):2443—53. https://doi.org/10.1210/jc.2017-00138.

[58] Zhang H, Liu Y, Yu B, Lu R. An optimized TRIzol-based method for isolating RNA from adipose tissue. Biotechniques 2023;74(5):203—9. https://doi.org/10.2144/btn-2022-0120.

[59] Meiser J, Krämer L, Sapcariu SC, Battello N, Ghelfi J, D'Herouel AF, et al. Pro-inflammatory macrophages sustain pyruvate oxidation through pyruvate dehydrogenase for the synthesis of itaconate and to enable cytokine expression. J Biol Chem 2016;291(8):3932—46. https://doi.org/10.1074/jbc.M115.676817.

[60] More TH, Mozafari B, Märtens A, Herr C, Lepper PM, Danziger G, et al. Plasma metabolome alterations discriminate between COVID-19 and non-COVID-19 pneumonia. Metabolites 2022;12(11). https://doi.org/10.3390/metabo12111058.

[61] He W, Henne A, Lauterbach M, Geißmar E, Nikolka F, Kho C, et al. Mesaconate is synthesized from itaconate and exerts immunomodulatory effects in macrophages. Nat Metab 2022;4(5):524—33. https://doi.org/10.1038/s42255-022-00565-1.

[62] Hiller K, Hangebrauk J, Jäger C, Spura J, Schreiber K, Schomburg D. Metabolite detector: comprehensive analysis tool for targeted and non-targeted GC/MS based metabolome analysis. Anal Chem 2009;81(9):3429—39. https://doi.org/10.1021/ac802689c.

[63] Dobin A, Davis CA, Schlesinger F, Drenkow J, Zaleski C, Jha S, et al. STAR: ultrafast universal RNA-seq aligner. Bioinformatics 2013;29(1):15—21. https://doi.org/10.1093/bioinformatics/bts635.

[64] Mölder F, Jablonski KP, Letcher B, Hall MB, Tomkins-Tinch CH, Sochat V, et al. Sustainable data analysis with Snakemake. F1000Research 2021;10:33. https://doi.org/10.12688/f1000research.29032.1.

[65] Love MI, Huber W, Anders S. Moderated estimation of fold change and dispersion for RNA-seq data with DESeq2. Genome Biol 2014;15(12). https://doi.org/10.1186/s13059-014-0550-8.

[66] Leek JT, Johnson WE, Parker HS, Jaffe AE, Storey JD. The SVA package for removing batch effects and other unwanted variation in high-throughput experiments. Bioinformatics 2012;28(6):882—3. https://doi.org/10.1093/bioinformatics/bts034.

[67] Ritchie ME, Phipson B, Wu D, Hu Y, Law CW, Shi W, et al. Limma powers differential expression analyses for RNA-sequencing and microarray studies. Nucleic Acids Res 2015;43(7):e47. https://doi.org/10.1093/nar/gkv007.

[68] Korotkevich G, Sukhov V, Budin N, Shpak B, Artyomov MN, Sergushichev A. Fast gene set enrichment analysis. bioRxiv 2021. https://doi.org/10.1101/060012.

[69] Liberzon A, Birger C, Thorvaldsdóttir H, Ghandi M, Mesirov JP, Tamayo P. The molecular signatures database hallmark gene set collection. Cell Systems 2015;1(6):417—25. https://doi.org/10.1016/j.cels.2015.12.004.

[70] Fulton DL, Sundararajan S, Badis G, Hughes TR, Wasserman WW, Roach JC, et al. TFCat: the curated catalog of mouse and human transcription factors. Genome Biol 2009;10(3). https://doi.org/10.1186/gb-2009-10-3-r29.

[71] Uhlén M, Fagerberg L, Hallström BM, Lindskog C, Oksvold P, Mardinoglu A, et al. Tissue-based map of the human proteome. Science 2015;347(6220). https://doi.org/10.1126/science.1260419.

[72] Moyer BJ, Rojas IY, Kerley-Hamilton JS, Hazlett HF, Nemani KV, Trask HW, et al. Inhibition of the aryl hydrocarbon receptor prevents Western diet-induced obesity. Model for AHR activation by kynurenine via oxidized-LDL, TLR2/4, TGFβ, and Ido1. Toxicol Appl Pharmacol 2016;300:13—24. https://doi.org/10.1016/j.taap.2016.03.011.

[73] Choi Y, Kim Y, Park S, Lee KW, Park T. Indole-3-carbinol prevents diet-induced obesity through modulation of multiple genes related to adipogenesis, thermogenesis or inflammation in the visceral adipose tissue of mice. J Nutr Biochem 2012;23(12):1732—9. https://doi.org/10.1016/j.jnutbio.2011.12.005.

[74] Li H, Xie Z, Lin J, Song H, Wang Q, Wang K, et al. Transcriptomic and metabonomic profiling of obesity-prone and obesity-resistant rats under high fat diet. J Proteome Res 2008;7(11):4775—83. https://doi.org/10.1021/pr800352k.

[75] Scott, C., Guilliams, M., n.d. Liver Cell Atlas. https://www.livercellatlas.org/index.php. [accessed February 20, 2024].

[76] Weichhart T, Hengstschläger M, Linke M. Regulation of innate immune cell function by mTOR. Nat Rev Immunol 2015;15(10):599—614. https://doi.org/10.1038/nri3901.

[77] Marchingo JM, Cantrell DA. Protein synthesis, degradation, and energy metabolism in T cell immunity. Cell Mol Immunol 2022:303—15. https://doi.org/10.1038/s41423-021-00792-8.

[78] Van den Bossche J, Baardman J, de Winther MPJ. Metabolic characterization of polarized M1 and M2 bone marrow-derived macrophages using real-time extracellular flux analysis. JoVE 2015;105:1—7. https://doi.org/10.3791/53424.

[79] Moreno-Vedia J, Girona J, Ibarretxe D, Masana L, Rodríguez-Calvo R. Unveiling the role of the fatty acid binding protein 4 in the metabolic-associated fatty liver disease. Biomedicines 2022. https://doi.org/10.3390/biomedicines10010197.

[80] Ranjit S, Boutet E, Gandhi P, Prot M, Tamori Y, Chawla A, et al. Regulation of fat specific protein 27 by isoproterenol and TNF-α to control lipolysis in murine adipocytes. J Lipid Res 2011;52(2):221—36. https://doi.org/10.1194/jlr.M008771.

[81] The Lancet Gastroenterology & Hepatology. Obesity: another ongoing pandemic. Lancet Gastroenterol Hepatol 2021;411. https://doi.org/10.1016/S2468-1253(21)00143-6.

[82] Meldrum DR, Morris MA, Gambone JC. Obesity pandemic: causes, consequences, and solutions—but do we have the will? Fertil Steril 2017:833—9. https://doi.org/10.1016/j.fertnstert.2017.02.104.

[83] Carambia A, Schuran FA. The aryl hydrocarbon receptor in liver inflammation. Semin Immunopathol 2021;43:563—75. https://doi.org/10.1007/s00281-021-00867-8/Published.

[84] Girer NG, Tomlinson CR, Elferink CJ. The aryl hydrocarbon receptor in energy balance: the road from dioxin-induced wasting syndrome to combating obesity with Ahr ligands. Int J Mol Sci 2020:1—13. https://doi.org/10.3390/ijms2201.

[85] Li Y, Innocentin S, Withers DR, Roberts NA, Gallagher AR, Grigorieva EF, et al. Exogenous stimuli maintain intraepithelial lymphocytes via aryl hydrocarbon receptor activation. Cell 2011;147(3):629—40. https://doi.org/10.1016/j.cell.2011.09.025.

[86] Furumatsu K, Nishiumi S, Kawano Y, Ooi M, Yoshie T, Shiomi Y, et al. A role of the aryl hydrocarbon receptor in attenuation of colitis. Dig Dis Sci 2011;56(9):2532—44. https://doi.org/10.1007/s10620-011-1643-9.

[87] Van den Bossche J, O'Neill LA, Menon D. Macrophage immunometabolism: where are we (going)? Trends Immunol 2017;38(6):395—406. https://doi.org/10.1016/j.it.2017.03.001.

[88] Heo MJ, Suh JH, Lee SH, Poulsen KL, An YA, Moorthy B, et al. Aryl hydrocarbon receptor maintains hepatic mitochondrial homeostasis in mice. Mol Metabol 2023;72. https://doi.org/10.1016/j.molmet.2023.101717.

[89] Turrens JF. Mitochondrial formation of reactive oxygen species. J Physiol 2003;552(2):335—44. https://doi.org/10.1113/jphysiol.2003.049478.

[90] Veith A, Moorthy B. Role of cytochrome P450s in the generation and metabolism of reactive oxygen species. Curr Opin Toxicol 2018;118(24):6072—8. https://doi.org/10.1002/cncr.27633.Percutaneous.

[91] Goetzman ES, Prochownik EV. The role for myc in coordinating glycolysis, oxidative phosphorylation, glutaminolysis, and fatty acid metabolism in normal and neoplastic tissues. Front Endocrinol 2018;9(APR). https://doi.org/10.3389/fendo.2018.00129.

[92] Morita M, Gravel SP, Chénard V, Sikström K, Zheng L, Alain T, et al. MTORC1 controls mitochondrial activity and biogenesis through 4E-BP-dependent translational regulation. Cell Metabol 2013;18(5):698—711. https://doi.org/10.1016/j.cmet.2013.10.001.

[93] Yeudall S, Upchurch CM, Seegren PV, Pavelec CM, Greulich J, Lemke MC, et al. Macrophage acetyl-CoA carboxylase regulates acute inflammation through control of glucose and lipid metabolism. Sci Adv 2022:1—19. https://doi.org/10.1126/sciadv.abq1984.

[94] Dominguez M, Brüne B, Namgaladze D. Exploring the role of ATP-citrate lyase in the immune system. Front Immunol 2021. https://doi.org/10.3389/fimmu.2021.632526.

[95] Wculek SK, Heras-Murillo I, Mastrangelo A, Mañanes D, Galán M, Miguel V, et al. Oxidative phosphorylation selectively orchestrates tissue macrophage homeostasis. Immunity 2023;56(3):516—530.e9. https://doi.org/10.1016/j.immuni.2023.01.011.

[96] Stienstra R, Saudale F, Duval C, Keshtkar S, Groener JEM, Van Rooijen N, et al. Kupffer cells promote hepatic steatosis via interleukin-1β-dependent suppression of peroxisome proliferator-activated receptor α activity. Hepatology 2010;51(2):511—22. https://doi.org/10.1002/hep.23337.

[97] Tosello-Trampont AC, Landes SG, Nguyen V, Novobrantseva TI, Hahn YS. Kuppfer cells trigger nonalcoholic steatohepatitis development in diet-induced mouse model through tumor necrosis factor-α production. J Biol Chem 2012;287(48):40161—72. https://doi.org/10.1074/jbc.M112.417014.

[98] Park SJ, Garcia Diaz J, Um E, Hahn YS. Major roles of kupffer cells and macrophages in NAFLD development. Front Endocrinol 2023. https://doi.org/10.3389/fendo.2023.1150118.

[99] Schaum N, Karkanias J, Neff NF, May AP, Quake SR, Wyss-Coray T, et al. Single-cell transcriptomics of 20 mouse organs creates a Tabula Muris. Nature 2018;562(7727):367—72. https://doi.org/10.1038/s41586-018-0590-4.

[100] Angulo P, Kleiner DE, Dam-Larsen S, Adams LA, Bjornsson ES, Charatcharoenwitthaya P, et al. Liver fibrosis, but no other histologic features, is associated with long-term outcomes of patients with nonalcoholic fatty liver disease. Gastroenterology 2015;149(2):389—397.e10. https://doi.org/10.1053/j.gastro.2015.04.043.

[101] Fernandez-Salguero P, Pineau T, Hilbert DM, McPhail T, Lee SST, Kimura S, et al. Immune system impairment and hepatic fibrosis in mice lacking the dioxin-binding ah receptor. Annu Rev Immunol 1995;21(5):722—6. https://doi.org/10.1126/science.7732381.

[102] Li C, Liu Y, Dong Z, Xu M, Gao M, Cong M, et al. TCDD promotes liver fibrosis through disordering systemic and hepatic iron homeostasis. J Hazard Mater 2020;395. https://doi.org/10.1016/j.jhazmat.2020.122588.

[103] Pierre S, Chevallier A, Teixeira-Clerc F, Ambolet-Camoit A, Bui LC, Bats AS, et al. Aryl hydrocarbon receptor-dependent induction of liver fibrosis by dioxin. Toxicol Sci 2014;137(1):114—24. https://doi.org/10.1093/toxsci/kft236.

[104] Duval C, Blanc E, Coumoul X. Aryl hydrocarbon receptor and liver fibrosis. Curr Opin Toxicol 2018;8:8—13. https://doi.org/10.1016/j.cotox.2017.11.010.

[105] Yan J, Tung HC, Li S, Niu Y, Garbacz WG, Lu P, et al. Aryl hydrocarbon receptor signaling prevents activation of hepatic stellate cells and liver fibrogenesis in mice. Gastroenterology 2019;157(3):793—806.e14. https://doi.org/10.1053/j.gastro.2019.05.066.

[106] Pradere JP, Kluwe J, De Minicis S, Jiao JJ, Gwak GY, Dapito DH, et al. Hepatic macrophages but not dendritic cells contribute to liver fibrosis by promoting the survival of activated hepatic stellate cells in mice. Hepatology 2013;58(4):1461—73. https://doi.org/10.1002/hep.26429.

[107] Vila IK, Badin PM, Marques MA, Monbrun L, Lefort C, Mir L, et al. Immune cell toll-like receptor 4 mediates the development of obesity- and endotoxemia-associated adipose tissue fibrosis. Cell Rep 2014;7(4):1116—29. https://doi.org/10.1016/j.celrep.2014.03.062.

[108] Madsen DH, Leonard D, Masedunskas A, Moyer A, Jürgensen HJ, Peters DE, et al. M2-like macrophages are responsible for collagen degradation through a mannose receptor-mediated pathway. J Cell Biol 2013;202(6):951—66. https://doi.org/10.1083/jcb.201301081.

[109] Walisser JA, Glover E, Pande K, Liss AL, Bradfield CA. Aryl hydrocarbon receptor-dependent liver development and hepatotoxicity are mediated by different cell types. Proc Natl Acad Sci USA 2005;102(49):17858—63. https://doi.org/10.1073/pnas.0504757102.

